Published in final edited form as:
Nat Metab. 2019 January ; 1(1): 111–124. doi:10.1038/s42255-018-0005-8.

Transferrin receptor 2 controls bone mass and pathological bone formation via BMP and Wnt signaling

Martina Rauner[#1,2], **Ulrike Baschant**[#1,2], **Antonella Roetto**[3], **Rosa Maria Pellegrino**[3], **Sandra Rother**[4], **Juliane Salbach-Hirsch**[1,2], **Heike Weidner**[1,2], **Vera Hintze**[4], **Graeme Campbell**[5], **Andreas Petzold**[6], **Regis Lemaitre**[7], **Ian Henry**[8], **Teresita Bellido**[9], **Igor Theurl**[10], **Sandro Altamura**[11], **Silvia Colucci**[11], **Martina U. Muckenthaler**[11], **Georg Schett**[12], **Davide Komla Ebri**[13], **J. H. Duncan Bassett**[13], **Graham R. Williams**[13], **Uwe Platzbecker**[2,14,15], and **Lorenz C. Hofbauer**[1,2,15,16]

[1]Department of Medicine III, Technische Universität Dresden, Dresden, Germany

[2]Center for Healthy Aging, Technische Universität Dresden, Dresden, Germany

[3]Department of Clinical and Biological Science, University of Torino, Torino, Italy

[4]Institute of Materials Science, Max Bergmann Center of Biomaterials, Technische Universität Dresden, Dresden, Germany

[5]Institute of Biomechanics, Hamburg University of Technology, Hamburg, Germany

[6]Deep Sequencing, Biotechnology Center, Technische Universität Dresden, Dresden, Germany

[7]Max Planck Institute for Cell Biology and Genetics, Protein Unit, Dresden, Germany

[8]Max Planck Institute for Cell Biology and Genetics, Scientific Computing Facility, Dresden, Germany

[9]Department of Anatomy and Cell Biology and Department of Medicine, Division of Endocrinology, School of Medicine, Indiana University, Indianapolis, IN, USA

[10]Department of Internal Medicine VI, Medical University of Innsbruck, Innsbruck, Austria

Corresponding author: Martina Rauner, PhD, Division of Endocrinology, Diabetes and Bone Diseases, Department of Medicine III, Technische Universität Dresden, 01307 Dresden, Germany, Tel: +49 351 458 4206, martina.rauner@ukdd.de.

Authorship contributions

MR, UB, AR, JSH, SR, UP, and LCH designed experiments. MR, UB, AR, RMP, JSH, HW, SR, GC, RB, AP, RL, IH, SC, DKE performed experiments and analyzed data. TB, SA, SC, MM and IT provided mouse bone samples. MR, UB, AR, JSH, HW, SR, VH, IH, TB, MM, JHDB, GRW, GS, IT, UP, and LCH interpreted the data and provided critical comments to the manuscript. MR, UB, and LCH wrote the manuscript. All authors provided critical review of the manuscript.

Competing interests

The Technische Universität Dresden holds a patent for the use of Tfr2-ECD to treat heterotopic ossification and other related bone excess diseases (PCT/EP2018/065846). Moreover, a patent application has been filed at the European Patent Office for the use of Tfr2 blockade for the treatment of bone and hematological diseases (#18 177 441.5, 19.06.2018). MR, UB, UP, and LCH are the inventors of both patents. IT is a consultant for Kymab Ltd.
The other authors declare no competing interests.

Data availability statement

All data sets generated during the current study are available from the corresponding author upon request. A Life Science Reporting Summary is available.

Europe PMC Funders Author Manuscripts

[11]Department of Pediatric Hematology, Oncology and Immunology, University of Heidelberg, Heidelberg, Germany

[12]Department of Internal Medicine 3, Friedrich-Alexander-University Erlangen-Nuremberg (FAU) and University Hospital Erlangen, Erlangen, Germany

[13]Molecular Endocrinology Laboratory, Department of Medicine, Imperial College London, London W12 0NN, United Kingdom

[14]Department of Medicine II, University Clinic Leipzig, Germany

[15]German Cancer Consortium (DKTK) Partner Site Dresden, Dresden, Germany

[16]Center for Regenerative Therapies Dresden, Technische Universität Dresden, Dresden, Germany

[#] These authors contributed equally to this work.

Europe PMC Funders Author Manuscripts

Abstract

Transferrin receptor 2 (Tfr2) is mainly expressed in the liver and controls iron homeostasis. Here, we identify Tfr2 as a regulator of bone homeostasis that inhibits bone formation. Mice lacking Tfr2 display increased bone mass and mineralization independent of iron homeostasis and hepatic Tfr2. Bone marrow transplantation experiments and studies of cell-specific Tfr2 knockout mice demonstrate that Tfr2 impairs BMP-p38MAPK signaling and decreases expression of the Wnt inhibitor sclerostin specifically in osteoblasts. Reactivation of MAPK or overexpression of sclerostin rescues skeletal abnormalities in Tfr2 knockout mice. We further show that the extracellular domain of Tfr2 binds BMPs and inhibits BMP-2-induced heterotopic ossification by acting as a decoy receptor. These data indicate that Tfr2 limits bone formation by modulating BMP signaling, possibly through direct interaction with BMP either as a receptor or as a co-receptor in a complex with other BMP receptors. Finally, the Tfr2 extracellular domain may be effective in the treatment of conditions associated with pathological bone formation.

Iron is indispensable for red blood cell production, bacterial defense, and cellular respiration1, however, iron excess is cytotoxic. Therefore, systemic iron levels are maintained in a narrow range to avoid iron deficiency and anemia, or iron overload leading to multi-organ damage. Amongst other organs, bone is highly susceptible to changes in iron homeostasis. Bone mineral density is negatively associated with systemic iron concentrations2 and patients suffering from hereditary hemochromatosis, a disorder characterized by iron overload, develop premature osteoporosis3. Despite these observations, the relationship between iron homeostasis and bone turnover remains largely unexplored.

Systemic iron concentrations are maintained by balancing dietary iron absorption and iron recycling from the reticuloendothelial system1. Hepcidin is a hepatic peptide hormone and key regulator of iron homeostasis4. By binding to ferroportin, an iron exporter, hepcidin causes the internalization and degradation of ferroportin, thereby limiting iron export into the circulation. Dysregulation of this mechanism leads to iron overload. Accordingly,

mutations in the gene encoding hepcidin or hepcidin-regulating genes cause hereditary hemochromatosis5.

Transferrin receptor 2 (Tfr2) is a key regulator of hepcidin. Similar to humans, mice with global or liver-specific deletion of *Tfr2* accumulate iron in the liver6–9. Tfr2 is proposed to control iron homeostasis by regulating hepcidin expression and has two isoforms: Tfr2α, which represents the full-length protein and regulates iron homeostasis in the liver, and Tfr2β, which lacks the intracellular and transmembrane domains and plays an important role in iron efflux in the spleen8. To date, the mechanisms whereby Tfr2 senses and regulates systemic iron concentrations remain incompletely understood. However, holo-transferrin can bind Tfr2 and prolong its half-life10. Thus, Tfr2 has been postulated to sense circulating iron and activate hepcidin in response to elevated transferrin saturation.

Tfr2-deficient hepatocytes have reduced bone morphogenetic protein (BMP) and p38MAPK/ERK signaling11–13, implicating these pathways in its signal transduction. Although BMP signaling is mostly known for its critical role in bone development and postnatal bone homeostasis14, it has also emerged as an important regulator of iron homeostasis. Deficiency of several components of the BMP pathway (*Bmpr1a, Bmpr2, Acvr1, Acvr2a, Smad4, Bmp2, Bmp6*) or their pharmacological inhibition result in iron overload15–20. Moreover, hemojuvelin, another regulator of hepcidin expression, has been identified as a hepatic BMP co-receptor16, further linking BMP signaling to iron homeostasis. Importantly, activating mutations in one of the BMP receptors that controls iron homeostasis, *ACVR1*, cause a rare human disorder, fibrodysplasia ossificans progressiva (FOP), which is characterized by excessive heterotopic ossification21. Thus, balancing BMP signaling is necessary to maintain bone and iron homeostasis in a physiological range.

Recent evidence indicates Tfr2 is not restricted to the liver, but is also expressed in erythroid progenitors to ensure their proper differentiation8,22,23. As BMP signaling has a critical role in the skeleton14,24, we hypothesized that Tfr2 may possess additional extrahepatic functions and regulate bone homeostasis. Here, we demonstrate that Tfr2 is a novel negative regulator of bone turnover. By binding BMP ligands, Tfr2 activates p38MAPK signaling in osteoblasts to induce expression of the Wnt inhibitor sclerostin and limit bone formation. Finally, by taking advantage of the BMP-binding property of the Tfr2 extracellular domain, we show that this protein fragment effectively inhibits heterotopic ossification in two preclinical models, suggesting it may also be efficacious to treat disorders of pathological bone formation.

Results

Tfr2-deficiency leads to high bone mass

To investigate whether the iron-sensing receptor Tfr2 regulates bone homeostasis, we studied $Tfr2^{-/-}$ mice, which are iron overloaded. Consistent with previous reports8,25, the transferrin saturation, serum iron and ferritin concentrations, and iron content in the liver were increased in $Tfr2^{-/-}$ mice compared to wild-type (WT) mice (Suppl. Fig 1a-d). In addition, atomic absorptiometry revealed a higher iron content in the cortical bone of $Tfr2^{-/-}$

mice (Suppl. Fig. 1e). As iron overload is associated with bone loss3, we expected a decreased bone volume in *Tfr2*$^{-/-}$ mice. However, in contrast to the low bone mass phenotype of mice with diet-induced iron overload and in different mouse models of hemochromatosis, including *Hfe*$^{-/-}$ mice26 and *Fpn*^{C326S} mutant mice27 (Suppl. Fig. 2a-c), *Tfr2*$^{-/-}$ mice displayed a 1.5-3-fold higher trabecular bone volume in the femur and the vertebrae and a 1.5-fold higher cortical bone density compared to WT controls (Fig. 1a-b). High bone mass was independent of sex and declined with age (Suppl. Fig. 3a-b). At a structural level, *Tfr2*$^{-/-}$ vertebrae had increased trabecular number (Tb.N) and thickness (Tb.Th) and decreased separation (Tb.Sp) (Fig. 1c-e). Furthermore, *Tfr2*$^{-/-}$ mice had increased trabecular bone micro-mineralization density (Suppl. Fig. 3c), which together with the increased bone volume enhanced bone strength (Fig. 1f).

We performed dynamic and static histomorphometry to determine whether the high bone mass phenotype was a consequence of increased bone formation or decreased bone resorption. *Tfr2* deficiency resulted in an increase in both osteoblast and osteoclast parameters. The bone formation rate and the serum concentration of the bone formation marker pro-collagen type I N-terminal peptide (P1NP) were elevated more than two-fold in *Tfr2*$^{-/-}$ mice, and the number of osteoclasts and serum concentration of the bone resorption marker C-terminal telopeptide of type I collagen (CTX) were similarly increased (Fig. 1g-l). The high bone turnover was present in both males and females at all ages studied (Suppl. Fig. 3d-e). Interestingly, *Tfr2*$^{-/-}$ mice were not protected from ovariectomy-induced bone loss, but lost even more bone than WT mice (Fig. 1m). Taken together, these data demonstrate that Tfr2 does not only control iron homeostasis, but also bone turnover.

High bone mass in *Tfr2*-deficient mice is independent of hepatic iron status or *Tfr2* expression in the liver

As *Tfr2*$^{-/-}$ mice have iron overload and high bone mass, whereas iron overload is commonly associated with decreased bone mass3,28, we investigated whether abnormal iron metabolism contributes to the skeletal phenotype in *Tfr2*$^{-/-}$ mice. Thus, *Tfr2*$^{-/-}$ mice received an iron-free diet for 8 weeks from weaning or were treated with the iron-chelator deferoxamine for three weeks from 10 weeks of age. Despite successful iron depletion by both regimens, bone mass remained elevated in *Tfr2*$^{-/-}$ mice (Fig. 2a-d), indicating the high bone mass phenotype in *Tfr2*$^{-/-}$ mice is independent of the hepatic iron status.

To corroborate these findings, we studied two distinct *Tfr2* mutant mouse models, which globally lack *Tfr2β* but have contrasting *Tfr2α* expression that results in divergent abnormalities of iron homeostasis8: *Tfr2* knock-in mice (KI) globally lack *Tfr2β* but have normal *Tfr2α* and thus normal iron parameters. By contrast, hepatocyte-specific *Tfr2* knock-out (LCKO) mice globally lack *Tfr2β*, and have *Tfr2α* deficiency restricted to the liver, but are severely iron-overloaded. Both models had comparable bone volume fractions compared to controls (Fig. 2e-f), indicating that neither *Tfr2β* nor hepatic *Tfr2α* play a role in the control of bone homeostasis.

Tfr2-deficiency in osteoblasts drives the high bone mass phenotype

To explore whether Tfr2 regulates bone mass directly via its expression in skeletal cells, we determined expression of *Tfr2α* and *Tfr2β* in various mouse tissues. As expected, *Tfr2α* was predominantly expressed in the liver with the next highest expression in femoral cortical bone (Suppl. Fig. 4a). *Tfr2β* mRNA expression was also detected in femoral cortical bone, although at a much lower level (C_T value spleen (positive control): 26, C_T value bone: 32). Using an antibody that binds to the extracellular domain of Tfr2 and thus detects both Tfr2α and Tfr2β isoforms, we confirmed expression of Tfr2 in vertebral bone sections, showing Tfr2-positive osteoclasts, osteoblasts, and osteocytes (Fig. 3a, d). Staining of bone sections from *Tfr2*$^{-/-}$ mice showed no non-specific binding of the Tfr2 antibody (Suppl. Fig. 3b). Osteoclasts and osteoblasts differentiated from the bone marrow of WT mice both expressed *Tfr2α* and *Tfr2β* mRNA transcripts *ex vivo* but expression of *Tfr2β* was very low in each cell type (data for *Tfr2β* not shown). *Tfr2α* was readily detectable in osteoclasts and osteoblasts, with peak levels of expression in mature osteoclasts (day 7/7) and in immature osteoblasts (day 7/21) (Fig. 3b, e). Immunocytochemistry confirmed Tfr2 expression in osteoclasts and osterix-expressing osteoblasts that were differentiated *ex vivo* (Fig. 3c, f). Subcellular fractioning of osteoblasts further localized the majority of Tfr2 to the membrane fraction (Fig. 3g). A low signal was also detected in the cytoplasm.

To determine if Tfr2 in osteoclasts or in osteoblasts regulates bone turnover, we performed reciprocal bone marrow transplantations. In WT and *Tfr2*$^{-/-}$ mice, bone marrow transplantation had no effect on vertebral or femoral bone volume irrespective of donor genotype (Fig. 3h), suggesting that Tfr2 deficiency in the hematopoietic compartment is not responsible for the high bone mass phenotype in *Tfr2*$^{-/-}$ mice. Consistent with these findings, deletion of *Tfr2* specifically in the myeloid lineage (*Lysm-cre*) and in mature osteoclasts (*Ctsk-cre*) did not affect bone volume at the spine (Fig. 3i). Femoral bone volume, however, was decreased in *Tfr2*$^{f/f}$*;Lysm-cre* mice, but not in *Tfr2*$^{f/f}$*;Ctsk-cre* mice (Suppl. Fig. 5a). By contrast, deletion of *Tfr2* in osteoblast progenitors, in which *Tfr2* expression is highest, increased bone mass at the femur and spine (Fig. 3j), increased trabecular number, and decreased trabecular separation (Fig. 3k). Bone formation was increased in *Tfr2*$^{f/f}$*;Osx-cre*, as reflected by higher serum P1NP levels (Fig. 3l) and a higher bone formation rate (Fig. 3m). Finally, deletion of *Tfr2* in osteoblasts did not change osteoclast numbers, but tended to increase serum levels of CTX (Fig. 3n-o). Consistent with published *Tfr2*$^{f/f}$*;Lysm-cre* mice29, *Tfr2*$^{f/f}$*;Ctsk-cre* and *Tfr2*$^{f/f}$*;Osx-cre* mice also showed a normal liver iron content (Suppl. Fig. 5b-c). Taken together, these data indicate that Tfr2 predominantly in osteoblasts regulates bone formation, but does not contribute to systemic iron homeostasis.

Tfr2-deficiency in osteoblasts attenuates BMP-MAPK signaling and results in decreased expression of Wnt inhibitors

As the data indicate a direct role for Tfr2 in osteoblasts, we performed genome-wide RNA sequencing analysis using primary osteoblasts from WT and *Tfr2*$^{-/-}$ mice to identify signaling pathways affected by deletion of *Tfr2*. A total of 5,841 differentially expressed genes (DEGs) were identified (Suppl. Data Set 1). We performed gene ontology analysis to determine the biological processes affected by *Tfr2* deficiency (complete list in Suppl. Table 1). Genes upregulated in *Tfr2*$^{-/-}$ osteoblasts belonged to the biological processes of negative

regulation of protein secretion and muscle systems. By contrast, genes involved in ossification, extracellular matrix organization, negative regulation of Wnt signaling, and Smad phosphorylation were downregulated in *Tfr2*$^{-/-}$ osteoblasts (Suppl. Fig. 6a). These data are consistent with molecular function and cellular component analyses, which revealed underrepresentation of genes involved in glycosaminoglycan and heparin binding, and BMP receptor binding as well as proteinaceous extracellular matrix and collagen formation (Suppl. Fig. 6a). Gene set enrichment analysis further demonstrated underrepresentation of genes involved in late osteoblastic differentiation and Wnt signaling, the latter associated with marked suppression of the Wnt inhibitor Dickkopf-1 (*Dkk1*) (Suppl. Fig. 6b-c). The complete list of significantly enriched gene sets is provided in the Suppl. Table 2.

Dkk1 and *Sost* (encoding the Wnt inhibitor sclerostin) were among the 25 most downregulated genes in *Tfr2*$^{-/-}$ osteoblasts *ex vivo* (Fig. 4a). Reduced expression of the two Wnt inhibitors was verified by qPCR and is consistent with increased expression of the Wnt target genes (*Axin2, Lef1, Cd44*) (Suppl. Fig 6c). *Dkk1* and *Sost* mRNA levels were also down-regulated in osteoblasts obtained from *Tfr2*$^{f/f}$*;Osx-cre* mice (Fig. 4b). Furthermore, expression of the osteocyte-associated genes *Phex* and *Dmp1* was decreased (Suppl. Fig 6c). Importantly, impaired expression of osteocytic markers was not due to reduced osteocyte number in *Tfr2*$^{-/-}$ bone (WT: 8.73±2.74 vs *Tfr2*$^{-/-}$: 9.77±0.85 osteocytes/bone volume fraction). Low concentrations of sclerostin and Dkk1 were further detected in the serum of *Tfr2*$^{-/-}$ mice (Fig. 4c), along with a greater proportion of osteoblasts/osteocytes with high expression of β-catenin and axin-2 (Fig. 4d). Finally, increased Wnt signaling was demonstrated in *Tfr2*$^{-/-}$ osteoblasts differentiated for 7 days using Western blot analysis of β-catenin (Fig. 4e).

Deep sequencing analysis also suggested decreased BMP signaling in *Tfr2*$^{-/-}$ osteoblasts, and recent studies indicate that *Sost* and *Dkk1* are downstream targets of BMP signaling30,31. Thus, we analyzed BMP target genes as well as the basal canonical (Smad) and non-canonical (MAPK) BMP signaling pathways in *Tfr2*$^{-/-}$ and WT osteoblasts. *Smad6* and *Id1* were significantly downregulated in *Tfr2*$^{-/-}$ osteoblasts, while *Id2* was not different (Suppl. Fig. 6c). Both, Smad 1/5/8 phosphorylation as well as ERK and p38 activation were decreased in *Tfr2*$^{-/-}$ compared to WT osteoblasts (Fig. 4e). Moreover, activation of BMP signaling following BMP-2 treatment demonstrated that Smad activation was delayed in *Tfr2*$^{-/-}$ osteoblasts, whereas activation of p38MAPK and ERK was persistently impaired (Fig. 4f-g). The reduced activation of non-canonical BMP signaling in *Tfr2*$^{-/-}$ osteoblasts was not restricted to BMP-2, but was also observed after BMP-4 and to a lesser extent BMP-6 stimulation (Fig. 4h, Suppl. Fig. 6d). Overall, *Tfr2* deficiency in osteoblasts results in impaired BMP signaling and increased activation of the Wnt pathway.

Reactivation of MAPK signaling or overexpression of sclerostin rescues high bone mass in *Tfr2*-deficiency

We next investigated the mechanisms underlying the Tfr2-mediated regulation of *Sost* expression, as this may be a major driver of the Tfr2-dependent effects on bone. Using *Tfr2*$^{-/-}$ osteoblasts *in vitro*, we confirmed the lack of induction of *Sost* expression after stimulation with BMP-2, BMP-4, and BMP-7 (Fig. 5a). Conversely, overexpression of *Tfr2*

in WT and *Tfr2*$^{-/-}$ osteoblasts markedly increased *Sost*, in particular following stimulation with BMP-2 (Fig. 5b, Suppl. Fig. 7a). To test the impact of sclerostin in producing the high bone mass in *Tfr2*$^{-/-}$ mice, we crossed *Tfr2*$^{-/-}$ mice with mice overexpressing human *SOST* in late osteoblasts/osteocytes (under the *Dmp1*-8kb-promoter). Overexpression of *SOST* significantly reduced the vertebral trabecular bone volume in *Tfr2*$^{-/-}$ mice (Fig. 5c) and normalized the bone formation rate (Fig. 5d). The osteoclast-covered bone surface was higher in *Tfr2*$^{-/-}$ and WT mice overexpressing *SOST* in osteoblasts/osteocytes compared to mice with normal *Sost* expression (Suppl. Fig. 7b).

Previous studies indicated that BMPs stimulate *Sost* expression via the BMP-Smad and BMP-MAPK pathways30,31. Because pERK and pp38 were most markedly reduced in *Tfr2*$^{-/-}$ osteoblasts, and neither Smad1 nor Smad4 overexpression in *Tfr2*$^{-/-}$ osteoblasts restored *Sost* mRNA levels (Suppl. Fig. 7c-f), we reactivated the MAPK pathways using anisomycin to rescue *Sost* expression. Treatment with anisomycin induced ERK and p38 phosphorylation (Suppl. Fig. 7g), and increased *Sost* mRNA expression in *Tfr2*$^{-/-}$ and WT osteoblasts: 19-fold in *Tfr2*$^{-/-}$ osteoblasts and 14-fold in WT osteoblasts at 100 nM anisomycin (Fig. 5e). Similarly, treatment of *Tfr2*$^{-/-}$ mice with anisomycin for 3 weeks increased serum levels of sclerostin (Fig. 5f), reduced osteoblast numbers (Fig. 5g) and decreased bone volume back to WT levels (Fig. 5h). Osteoclast numbers were not altered by anisomycin treatment (Suppl. Fig. 7h). Finally, we investigated which specific MAPK pathway, ERK or p38, regulates *Sost* expression. Only the overexpression of *Mapk14* (encoding for p38α), but not *Mapk1* (encoding for ERK2), restored reduced *Sost* levels in *Tfr2*$^{-/-}$ osteoblasts (Fig. 5i-j). Thus, Tfr2 controls bone mass by inducing *Sost* expression via the p38MAPK signaling pathway.

Tfr2 is a novel interaction partner of BMPs

Finally, we asked how Tfr2 can lead to impaired BMP-MAPK signal transduction in osteoblasts and therefore explored whether Tfr2 can act as a BMP receptor. We generated a protein fragment containing the extracellular domain of Tfr2 (Tfr2-ECD), confirmed its presence using SDS-PAGE and Western blot (Suppl. Fig. 8a), and performed surface plasmon resonance (SPR) analysis. Tfr2-ECD immobilized on the sensor chip bound BMPs-2, 4, 6 and 7 more avidly than holo-transferrin (Tf) (Fig. 6a, Suppl. Fig. 8b), the only known Tfr2 ligand10. BMPs-2, 4, and 6 also bound to Tfr2-ECD at high salt concentrations, which were used to reduce non-specific binding, even though at a lower level (Suppl. Fig. 8c). Tfr2-BMP binding was further verified using the inverse approach using Tfr2-ECD as an analyte and BMP-2 or BMP-4 immobilized on the sensor chip (Suppl. Fig. 8d-e). Using this approach, we determined K_d values for Tfr2/BMP-2 (488.0 ± 37.0 nM) and Tfr2/BMP-4 (409.1 ± 39.0 nM) binding via steady state analysis. Holo-Tf bound to Tfr2 at micromolar concentrations suggesting a K_d value in the micromolar range (Suppl. Fig. 8f). Holo-Tf and BMP-2 did not compete for binding to Tfr2, as the sequential injection of either BMP-2 followed by holo-Tf, or holo-Tf followed by BMP-2 did not change the initial binding response (Suppl. Fig. 8g-h). Interestingly, the concomitant injection of BMP-2 and holo-Tf led to a much stronger binding response to Tfr2 than either analyte alone (Fig. 6b). As BMPs normally signal through a receptor complex consisting of the type I and type II BMP receptors, we tested whether BMPRs bind to Tfr2-ECD. Both BMPR-IA and BMPR-II had a

binding response weaker than BMPs (Fig. 6a, Suppl. Fig. 8i). The physical interaction of Tfr2 and BMPR-IA was further investigated using a cell system in which they were both overexpressed. Their interaction was confirmed by co-immunoprecipitation and was not affected by the presence of BMP-2 (Suppl. Fig. 8j). BMP-2 binding to the Tfr2-ECD was further verified using a competitive sandwich ELISA with BMPR-IA as a control (Fig. 6c). Additional SPR experiments revealed that BMPR-IA competes with Tfr2 for BMP-2 binding, as adding increasing concentrations of BMPR-IA reduced the binding of BMP-2 to Tfr2-ECD (Fig. 6d). Of note, high nanomolar concentrations of BMPR-IA were required for competing with Tfr2/BMP-2.

We validated the BMP ligand binding property of Tfr2-ECD *in vivo* using a heterotopic ossification model. In this model, BMP-2 is injected into the anterior tibialis muscle of mice, which leads to muscular ossification32. While BMP-2 alone led to heterotopic ossification of the muscle in WT mice, the addition of Tfr2-ECD completely abrogated this effect (Fig. 6e, Suppl. Fig 9a-b), suggesting that Tfr2 binds BMP-2 and prevents it from binding to its cognate BMPR. Similar experiments in *Tfr2*$^{-/-}$ mice demonstrated increased heterotopic ossification following BMP-2 injection as compared to WT mice, which was significantly inhibited by co-application of Tfr2-ECD (Fig. 6e, Suppl. Fig 9a-b). Thus, in addition to confirming functional BMP-binding activity of the Tfr2-ECD *in vivo*, these data emphasize the role of Tfr2 as a negative regulator of ossification in a BMP-dependent context.

Tfr2-ECD potently inhibits heterotopic ossification in two distinct preclinical models

Due to the robust effect of the Tfr2-ECD to diminish BMP-2-induced heterotopic ossification, we compared Tfr2-ECD with palovarotene, a selective retinoic acid receptor-γ agonist that indirectly inhibits BMP signaling33 and is currently under clinical investigation for the treatment of FOP. Tfr2-ECD was either used as a single local treatment into the muscle or as a systemic treatment (i.p. injections every other day). Both regimens reduced BMP-2-induced heterotopic ossification in WT mice after two weeks with similar efficacy to daily palovarotene administration (Fig. 6f). Investigation of the chondrogenic phase of heterotopic ossification at day 8 in WT mice revealed that both systemic Tfr2-ECD and palovarotene treatment suppressed the number of chondrocytes and the production of cartilage (Suppl. Fig. 9c-d). No adverse effects of systemic Tfr2-ECD treatment were observed on blood counts, iron parameters, bone homeostasis or the gross morphology of internal organs (Suppl. Table 3). Finally, we tested both compounds in a model of trauma-potentiated heterotopic ossification, a frequent complication after trauma, blast injuries, or hip replacement surgeries. A single dose of Tfr2-ECD inhibited new bone formation in the muscle comparable to palovarotene (Fig. 6g). Daily treatment with ibuprofen, a frequent treatment of heterotopic ossification after hip surgeries34, did not prevent trauma-induced heterotopic ossification (Fig. 6g). These data indicate that Tfr2-ECD is a potent inhibitor of heterotopic ossification and represents a potential new therapeutic strategy for treating disorders of excessive bone formation.

Discussion

Using a series of genetically modified mice and *in vitro* analyses, these studies identify a new role for Tfr2 as a modulator of BMP and Wnt signaling in osteoblasts. Tfr2 interacts with BMP ligands and receptors, activates p38MAPK signaling, and induces expression of the Wnt inhibitor *Sost*. This in turn blocks canonical Wnt signaling, thereby limiting bone formation and bone mass accrual (Fig. 5k). Further, exploiting the BMP-binding property of the Tfr2-ECD in form of a decoy receptor shows promise as a novel therapeutic strategy to prevent heterotopic ossification (Fig. 6h), which is of particular interest as there are currently no specific treatments for congenital or trauma-induced heterotopic ossification.

Besides its well-known function in the regulation of systemic iron levels6–9, Tfr2 ensures proper erythropoiesis8,22,23. Our study has now identified a novel extrahepatic role of Tfr2, control of bone mass via direct actions in osteoblasts, even though minor effects in myeloid cells including early osteoclasts cannot be excluded. This appears to be a unique property of Tfr2 among the other iron-regulating proteins, as all other investigated mouse models of hemochromatosis display low bone mass. Accordingly, others have shown low bone mass in patients with *HFE*-dependent hemochromatosis3 and in *Hfe*- and hepcidin-deficient mice35,36. In both cases, suppressed bone formation was proposed as the main underlying mechanism of low bone mass35,37. However, as both *Hfe*- and hepcidin-deficient mice are iron-overloaded, it is unclear whether the low bone mass is an indirect result of the negative effects of iron overload, or whether *Hfe* and hepcidin exert direct actions in bone cells. Importantly, the high bone mass in *Tfr2*-deficient mice was independent of the iron status and the hepatic function of Tfr2, indicating Tfr2 has distinct roles in osteoblasts (i.e. control of matrix production) and hepatocytes (i.e. regulation of hepcidin expression and systemic iron homeostasis).

Even though Tfr2 has been known as a regulator of iron homeostasis for over 15 years, its mechanisms of action have remained elusive. Decreased levels of Smad1/5/8 and MAPK/ERK signaling in *Tfr2*-deficient hepatocytes suggested that BMP signaling may be involved11,13,38, but it remained unclear how Tfr2 activates BMP signaling. Previous studies in hepatocytes suggested that Tfr2 forms a ternary complex with Hfe and hemojuvelin to activate hepcidin expression12. Our data, however, provide *in vitro* and *in vivo* evidence, which demonstrates that Tfr2 can bind BMPs directly and activate downstream signaling. Binding of BMP-2 to Tfr2 was more than 10-fold higher than that of holo-Tf, the only known ligand for Tfr210. Compared to BMP-BMPR interactions39,40, BMP-Tfr2 binding was markedly lower, suggesting that Tfr2 may act to fine-tune BMP signaling. As our studies also showed a direct interaction of Tfr2 with BMPRs, it remains to be investigated whether Tfr2 binds BMPs alone or within a multi-receptor complex with BMPRs and/or other BMP co-receptors. Despite these first indications of Tfr2 being a BMP (co)-receptor, additional experiments will be required to define accurate binding affinities that account for stoichiometry, the possibility of receptor dimerization or oligomerization, and Tfr2-ECD purity. Interestingly, the combination of holo-Tf and BMP-2 bound much more avidly to Tfr2 than either holo-Tf or BMP-2 alone, suggesting that holo-Tf may exhibit significant Tfr2 binding only in the presence of BMPs. This may be of particular importance as hepatic endothelial cells have been identified as the main producers of BMP-2 and

BMP-6 that act locally on hepatocytes to control hepcidin expression and iron homeostasis41,42. While hemojuvelin has been recognized to transmit the signal of BMP-6 to modulate hepcidin expression, BMP-6 can still induce hepcidin expression in hemojuvelin knock-out mice43, suggesting that other receptors must be involved. Thus, the newly identified BMP-binding properties of Tfr2 may represent the missing link in the regulation of hepcidin via BMPs.

Our study further showed that BMP downstream signaling, in particular the BMP-p38MAPK pathway, is impaired in *Tfr2*$^{-/-}$ osteoblasts resulting in reduced expression of the canonical Wnt inhibitors *Dkk1* and *Sost*, which are both potent negative regulators of bone formation44–46. Recent work has shown that BMP-2 stimulates expression of *Dkk1* and *Sost* by activating BMP-dependent Smad signaling and, in the case of *Dkk1*, also through MAPK signaling via ERK and p3830,47. More recent studies, including our own show that *Sost* expression is also induced by p38MAPK signaling in osteoblasts30,48. Accordingly, anisomycin treatment, which activates all three MAPKs49, rescued *Sost* expression and restored bone mass in *Tfr2*$^{-/-}$ mice. Similar to the phenotype of *Tfr2*$^{-/-}$ mice and counterintuitive to the supportive actions of BMP signaling on osteoblastic bone formation, targeted disruption of *Bmpr1a* or *Acvr1* in osteoblasts impairs expression of *Sost* and results in high bone mass47,50. In addition, treatment of *Bmpr1a*-deficient calvaria with recombinant sclerostin *ex vivo* restored normal bone morphology47, similarly as overexpression of *SOST* in *Tfr2*$^{-/-}$ mice reduced bone volume back to WT levels. However, *Tfr2*-deficient mice do not fully phenocopy the skeletal phenotype of *Bmpr1a*- or *Sost*-deficient mice. Considering osteoblast/osteocyte-specific knock-out strains, deletion of all three genes leads to high bone mass. However, while *Bmpr1a*-conditional knock-out mice have a low bone turnover30,47,51, *Tfr2*-conditional knock-out mice have a high bone formation rate and normal osteoclast parameters, and *Sost*-conditional knock-out mice have a high bone formation rate52. Osteoclast parameters have not been reported in *Sost*-conditional knock-out mice, but are normal in *Sost*$^{-/-}$ mice44. While an increase in bone formation appears the predominant mechanism of high bone mass in *Tfr2*- and *Sost*-conditional knock-out mice, the main driver of high bone mass in *Bmpr1a*-conditional knock-out mice appears to be reduced osteoclastogenesis due to a low RANKL-to-OPG ratio in osteoblasts30,47. This mechanism was reported to be independent of Wnt signaling, as overexpression of *Sost* did not rescue the osteoclast phenotype in *Bmpr1a*-conditional knock-out mice47. By contrast, *Tfr2*$^{-/-}$ mice have elevated osteoclast numbers and an increased RANKL-to-OPG ratio (WT: 0.225±0.046, *Tfr2*$^{-/-}$: 0.696±0.120, n=4, p=0.0003), but similar to *Bmpr1a*-conditional knock-out mice, this phenotype was not rescued by *Sost* overexpression. Interestingly, deficiency of *Bmpr2* in osteoblasts results in high bone mass accompanied by a high bone formation rate and normal bone resorption53, suggesting that Tfr2 shares more similarities with Bmpr2 than Bmpr1a. Finally, *Bmpr1a*-conditional knock-out mice have disorganized bone matrix, leading to reduced bone strength54,55. This is in contrast to *Tfr2*$^{-/-}$ and *Sost*$^{-/-}$ mice, which both have normal bone matrix organization and increased bone strength44. Taken together, despite similarities, which propose Tfr2 acts in similar way or even in conjunction with BMPRs, additional pathways appear to mediate its effects on bone independent of BMP signaling. In sum, Tfr2 is clearly a critical regulator of *Sost* expression in osteoblasts and provides another link between BMP and Wnt signaling.

Finally, we show that the ability of the Tfr2-ECD to bind BMPs and act as a decoy receptor reduces heterotopic ossification in two distinct preclinical models. Heterotopic ossification is a serious and common medical complication after blast injuries, such as found in soldiers and civilians, burn victims, and recipients of total hip endoprostheses. Up to 30% of patients undergoing hip replacement surgery and 50% of severely wounded soldiers develop heterotopic ossification56,57. Extensive heterotopic ossification is also a hallmark of FOP, a rare human disease caused by an activating mutation in the BMP type I receptor *ACVR1*21. Since the identification of this mutation, BMP signaling has been implicated in the pathogenesis of heterotopic ossification. To date, therapeutic options for FOP and trauma-induced heterotopic ossification are limited. Radiation and non-steroidal anti-rheumatic drugs are frequently used to inhibit surgery-induced heterotopic ossification with varying success34. In our study, ibuprofen did not significantly reduce heterotopic ossification. In FOP, glucocorticoids are used to reduce inflammation during flare-ups. However, they do not block progressive ossification. Rapamycin, anti-activin antibodies, and palovarotene have recently been shown to reduce heterotopic ossification in preclinical models of FOP via different mechanisms33,58–60. Palovarotene indirectly interferes with the BMP pathway and is currently the only drug under clinical investigation. Both, local and systemic treatment with Tfr2-ECD inhibited heterotopic ossification to a similar extent as palovarotene. Systemic treatment with Tfr2-ECD did not show adverse effects on iron or bone metabolism within the 2 week treatment period, which is of relevance as mice lacking *Tfr2β*, which has a similar structure as Tfr2-ECD, have increased iron levels in the spleen8 and therefore, differences in iron metabolism may have been anticipated. In the future, longer and more extensive pharmacological studies are required to conclusively address the safety profile of Tfr2-ECD.

Taken together, we have uncovered Tfr2 as a novel regulator of bone mass via modulating the BMP-p38MAPK-Wnt signaling axis and identified Tfr2-ECD as a promising therapeutic option to treat heterotopic ossification and disorders of excessive bone formation.

Methods

Mice

Generation of $Tfr2^{-/-}$ mice and *Tfr2* knock-in (*Tfr2*-KI) mice, which only lack the *Tfr2β* isoform, were previously described8. Conditional *Tfr2* knock-out mice were generated on the background of the *Tfr2*-KI mouse (129X1/svJ), thereby producing cell-type specific *Tfr2α* knock-out mice which also lack *Tfr2β* globally. Liver-specific *Tfr2*-knock-out mice (LCKO) were generated using the albumin-cre (sv129 background). To delete *Tfr2α* in osteoblast precursors the doxycycline-repressible osterix-cre (*Osx-cre*) was used61. Breeding pairs and mice up to the age of 5 weeks were kept on doxycycline (0.5 g/l). For the deletion of *Tfr2α* in mature osteoclasts the cathepsin K cre (*Ctsk-cre*) was used62. Lysozyme M (*Lysm-cre*) was used for deletion of *Tfr2* in early osteoclasts63. $Tfr2^{f/f}$;*Osx-cre,* $Tfr2^{f/f}$;*Lysm-cre,* and $Tfr2^{f/f}$;*Ctsk-cre* mice were on a mixed sv129/C57BL/6 background. Littermates were used as controls.

To obtain *Tfr2*-deficient mice with an overproduction of human sclerostin, $Tfr2^{-/-}$ mice were crossed with *Dmp1-SOST* transgenic mice to obtain $Tfr2^{-/-}$;$Dmp1\text{-}SOST^{+/tg}$ mice64. The

production of ferroportin knock-in mice with a point mutation (C326S) and *Hfe* knock-out mice were described previously26,27. All mice were routinely genotyped using standard PCR protocols.

In vivo experiments

All animal procedures were approved by the institutional animal care committee and the Landesdirektion Sachsen. All mice were fed a standard diet with water *ad libitum* and were kept in groups of 5 animals per cage. Mice were exposed to a 12 h light/dark cycle and an air-conditioned room at 23 °C (no specific pathogen free room). Enrichment was provided in forms of cardboard houses and bedding material. Mice were randomly assigned to treatment groups and the subsequent analyses were performed in a blinded-fashion.

Bone phenotyping—Male and female *Tfr2*$^{-/-}$ and wild-type mice at 10-12 weeks of age were used. For the characterization of *Tfr2*$^{-/-}$ mice, older mice (6 and 12 months) were also used. Male *Tfr2*$^{f/f}$;*Osx-cre* and *Tfr2*$^{f/f}$;*Ctsk-cre* and the corresponding cre-negative littermate controls were sacrificed at 10-12 weeks for bone phenotype analysis.

Ovariectomy—Female 11-14-week-old WT or *Tfr2*$^{-/-}$ mice were bilaterally ovariectomized or sham operated. After four weeks, mice were sacrificed for further analyses. Each group consisted of 5-10 mice.

Iron-rich diet—WT animals received a 2% iron-enriched standard diet from weaning (14 days old) until sacrifice (8 weeks of treatment). Four-five mice per group.

Iron-free diet—Male *Tfr2*$^{-/-}$ and WT mice received an iron-free diet (Envigo, Italy) from weaning until 10 weeks of age. Control mice received a standard diet containing 0.2 g iron/kg food (GLOBAL DIET 2018, Envigo, Italy). Nine mice per group.

Iron chelation—Ten-week-old male *Tfr2*$^{-/-}$ and WT mice received daily intraperitoneal injections of 250 mg/kg DFO (Sigma, Germany, dissolved in PBS) or PBS for three weeks. This experiment was performed two independent times with 3-5 mice.

Full bone marrow transplantation—Bone marrow cells were isolated from 12-week-old male *Tfr2*$^{-/-}$ mice or WT controls. Two million cells were transplanted into lethally irradiated (8 Gy) male WT or *Tfr2*$^{-/-}$ mice by retro-orbital venous plexus injection. Engraftment efficiency was monitored every four weeks using flow cytometry. After 16 weeks, mice were sacrificed for bone analyses. This experiment was performed twice with each 7-12 mice per group.

Anisomycin treatment—Female 11-week-old WT and *Tfr2*$^{-/-}$ mice were treated with 5 mg/kg anisomycin (i.p.) 3x/week for three weeks. This experiment was performed twice with each 5 mice per group.

Heterotopic ossification (HO)—The HO model was performed according to Wosczyna et al32. Briefly, 2.5 µl of 1 mg/ml recombinant BMP-2 (Thermo Fisher) or 2.5 µl of 1 mg/ml Tfr2-ECD were mixed with 47.5 µl matrigel (BD Bioscience) on ice. For the local

combination treatment, 2.5 μl BMP-2 were mixed with 2.5 μl Tfr2-ECD and 45 μl matrigel. The matrigel-mixtures were injected into the midbelly of the tibialis anterior muscle of 10-week-old female WT and *Tfr2*-deficient mice. Some mice were treated daily with palovarotene through oral gavage using a previously published protocol58. Palovarotene (Hycultec) was dissolved in DMSO and diluted 1:4 with corn oil. Mice received palovarotene at a dose of 100 μg/mouse for the first five days and 50 μg/mouse for the remainder of the experiment (days 6-14). Two weeks after BMP-2 injection, the legs were harvested for analysis. This experiment was performed three times with 3-11 mice per group.

To analyze the *chondrogenic phase* of HO, we performed an experiment as described above that was terminated on day 8. This was performed once with 4-6 mice per group.

For *systemic Tfr2-ECD treatment*, WT mice were treated every other day with Tfr2-ECD intraperitoneally for two weeks. Mice received 250 μg Tfr2-ECD (10 mg/kg BW) per injection for the first 10 days after BMP-2/matrigel injection into the muscle and 125 μg per injection (5 mg/kg BW) for the remaining time. This experiment was performed once with 8-10 mice per group.

Drop-weight HO—This experiment was performed according to Liu et al. with minor modifications65. Female 10-12-week-old WT mice were anesthetized and placed on a ridge of a plastic container over which the right leg was bent so the femur was lying horizontally. Mice received an injection of 1 μg BMP-2 mixed in 50 μl matrigel. Afterwards, a stainless-steel ball of 16 g (16 mm diameter) was dropped from a distance of 80 cm height onto the quadriceps muscle. Mice either received a single dose of 1 μg Tfr2-ECD, which was co-injected with the BMP-2/matrigel mixture, or palovarotene (Hycultec), which was administered daily by oral gavage. Palovarotene was dissolved in DMSO and diluted 1:4 with corn oil. Mice received palovarotene at a dose of 100 μg/mouse for the first five days and 50 μg/mouse for the remainder of the experiment (days 6-21). One group of mice received ibuprofen via the drinking water at a dose of 100 mg/ml which was changed every other day66. Mice received methamizole (200 mg/kg) to reduce pain for the entire duration of the experiment. This experiment was performed twice with 6 mice per group.

Micro-CT, bone micromineralization density, and biomechanical testing

Bone microarchitecture was analyzed using the vivaCT40 (Scanco Medical, Switzerland). The femur and the fourth lumbar vertebra were imaged at a resolution of 10.5 μm with X-ray energy of 70 kVp, 114 mA, and an integration time of 200 ms. The trabecular bone in the femur was assessed in the metaphysis 20 slices below the growth plate using 150 slices. In the vertebral bone, 150 slices were measured between both growth plates. The cortical bone was determined in the femoral midshaft (150 slices). Pre-defined scripts from Scanco were used for the evaluation.

Bone micro-mineralization densities were determined by quantitative back scattered electron-scanning electron microscopy (qBSE-SEM). Neutral buffered formalin fixed fourth lumbar vertebrae (L4) from 12 week old male mice were embedded in methacrylate. Longitudinal block faces were cut through specimens, which were then polished and coated

with 25 nm of carbon using a high resolution sputter coater (Agar Scientific Stanstead UK). Samples were imaged using backscattered electrons at 20 kV, 0.4 nA and a working distance of 17 mm with a Tescan VEGA3 XMU (Tescan, Brno, Czech Republic) equipped with a Deben 24 mm 4-quadrant backscatter detector (Deben, Bury St. Edmunds, UK). Bone mineralization densities were determined by comparison to halogenated dimethacrylate standards, and an eight-interval pseudocolor scheme was used to represent the graduations of micro-mineralization, as previously described67.

Three-point bending of the femur was conducted to assess bone strength. The femurs were stored in 70% ethanol and rehydrated in PBS prior to testing. Mechanical testing was performed using the zwicki-Line from Zwick, Germany. Load was applied to the anterior side of the femoral shaft to measure the maximum load at failure (Fmax, N).

Bone histomorphometry

Mice were injected with 20 mg/kg calcein (Sigma) five and two days before sacrifice. Dynamic bone histomorphometry was performed as described previously68. Briefly, the third lumbar vertebra and tibia were fixed in 4% PBS-buffered paraformaldehyde and dehydrated in an ascending ethanol series. Subsequently, bones were embedded in methacrylate and cut into 7 μm sections to assess the fluorescent calcein labels. Unstained sections were analyzed using fluorescence microscopy to determine the mineralized surface/bone surface (MS/BS), the mineral apposition rate (MAR), and the bone formation rate/bone surface (BFR/BS) as well as the bone volume/total volume (BV/TV), trabecular number (Tb.N), trabecular separation (Tb.Sp), and trabecular thickness (Tb.Th).

To determine numbers of osteoclasts, the femur and fourth lumbar vertebra were decalcified for one week using Osteosoft (Merck), dehydrated, and embedded into paraffin. Tartrate-resistant acid phosphatase (TRAP) staining was used to assess the osteoclast surface per bone surface (Oc.S/BS). Bone sections were analyzed using the Osteomeasure software (Osteometrics, USA) following international standards.

To assess HO using the hematoxylin/eosin staining, the calves (HO) and thighs (drop weight) were decalcified, dehydrated and embedded into paraffin. Limbs were cut into 2 μm sections and stained with hematoxylin/eosin. For von Kossa/van Giemson and Safranin O staining, legs were not decalcified, embedded into methacrylate and cut into 4 μm thick sections.

Immunohistochemistry

For immunohistochemical analysis, paraffin sections from WT and *Tfr2*$^{-/-}$ bones were dewaxed, rehydrated, and heat-retrieved of antigens. Endogenous peroxidase activity was blocked using 0.3% H_2O_2/PBS for 10 min at room temperature and non-specific binding sites using the blocking buffer of the VECTASTAIN Elite ABC Kit (VECTOR Laboratories) for 45 min at room temperature. Afterwards, sections were incubated with an anti-Tfr2 antibody (H-140, Santa Cruz), a β-catenin antibody (BD Bioscience) or an axin-2 antibody (#ab107613, Abcam) overnight at 4 °C. Subsequently, slides were treated with an anti-mouse secondary antibody conjugated to biotin and then developed utilizing avidin-conjugated HRP with diaminiobenzidine as substrate (DAKO). Slides were examined using

a Zeiss Axio Imager M.1 microscope. Two-hundred cells were counted per slide and graded according to no staining (0), weak staining (1), and strong staining (2).

Measurement of the iron content in the liver and bone

The iron concentration in the liver was determined using 20 mg of dried liver tissue as previously published8. The iron concentration in the bone was determined using atomic absorption spectroscopy (PerkinElmer Analyst 800) of dried bone tissue (bone marrow-flushed femur and tibia) as previously published69.

Serum analysis

The bone turnover markers C-terminal telopeptide (CTX) and pro-collagen type I N-terminal peptide (P1NP) were measured in the serum using ELISAs (IDS, Germany). Serum dickkopf-1 and BMP-2 were measured using ELISAs from R&D Systems (Germany). Mouse sclerostin was measured with an ELISA from Alpco (USA). Serum ferritin and iron were measured using routine methods for clinical analyses on a Roche Modular PPE analyzer. The transferrin saturation was determined using a total iron binding capacity kit from Randox.

Primary osteoclast culture

Osteoclasts were generated from the bone marrow of WT mice and seeded at a density of $1x10^6$ cells/cm^2. Alpha-MEM (Biochrom, Germany) with 10% FCS, 1% penicillin/streptomycin, and 25 ng/ml M-CSF (all from Life Technologies) was used for the first two days of differentiation. Afterwards, medium was supplemented with 30 ng/ml RANKL (Life Technologies) for the remainder of the culture (5-7 days). RNA was isolated at various time points and mature osteoclasts were used for immunofluorescence analysis.

Primary osteoblast culture

Primary murine osteoblasts were differentiated from the bone marrow using standard osteogenic medium in DMEM with 10% FCS, 1% penicillin/streptomycin (Life Technologies, Germany). RNA was isolated at various time points and day 7 osteoblasts were used for immunofluorescence analysis of Tfr2 and for the deep sequencing analysis.

Signaling studies—day 7 differentiated cells were treated with 50 ng/ml BMP-2, BMP-4 or BMP-6 for 0, 20, and 40 min and lysed in protein lysis buffer (at least two independent experiments with 3 n each). Anisomycin was used to activate MAPK signaling on day 7 differentiated osteoblasts. Cells were treated with 100 nM anisomycin for 20 min for subsequent protein analysis. For RNA isolation and detection of gene expression, cells were treated with different doses of anisomycin for 24 h (two independent experiments with 3 n each).

Overexpression—One μg of the pcDNA3.1 vector containing the murine *Tfr2* gene was transfected into 70-80% confluent cells using Fugene HD (Roche)8. An empty pcDNA3.1 vector was used as control. In addition, the overexpression vectors pCMV6-MAPK1 (ERK2), pCMV6-MAPK14 (p38α), pCMV6-Smad1, and pCMV6-Smad4 were purchased

from Origene to overexpress the respective signaling proteins. The pCMV6-Entry vector was used as control. Each experiment was performed once with cells from 4 different mice.

RNA isolation, RT and real-time PCR

RNA from cell cultures was isolated with the High Pure RNA Isolation Kit (Roche) and RNA from the bones of mice was isolated by crushing flushed bones (femur and tibia) in liquid nitrogen and collecting the bone powder in Trifast (Peqlab, Germany). Other organs were homogenized directly in Trifast using an ultraturrax (IKA, Germany). Five-hundred ng RNA were reverse transcribed using Superscript II (Invitrogen, Germany) und subsequently used for SYBR green-based real-time PCRs using a standard protocol (Life Technologies). The results were calculated using the ΔΔCT method and are presented in x-fold increase relative to β-actin (or *GAPDH* where indicated) mRNA levels.

Protein isolation and Western blot

Cells were lysed in a buffer containing 20 mM Tris/HCl pH 7.4, 1% SDS, and a protease inhibitor (complete mini, Roche, Germany). To isolate protein from tissues, the protein fraction of the Trifast procedure was used and further processed according to the manufacturer´s protocol. The protein concentration was determined using the BCA method (Pierce, Germany). Twenty µg of heat-denatured protein was loaded onto a 10% gel, separated, and transferred onto a 0.2 µm nitrocellulose membrane (Whatman, Germany). After blocking for 1 h with 5% non-fat dry milk or 2% BSA in Tris-buffered saline with 1% Tween-20 (TBS-T), membranes were incubated with primary antibodies to signaling proteins (Cell Signaling) overnight and washed three times with TBS-T. For the detection of Tfr2, the H-140 antibody from Santa Cruz (Germany) was used, which detects an epitope corresponding to amino acids 531-670. Other antibodies used were: lamin A/C (#sc-20681, Santa Cruz), connexin-43 (#3512, Cell Signaling), tubulin (#2146, Cell Signaling), GAPDH (#5G4, Hytest). Thereafter, membranes were incubated with the appropriate HRP-conjugated secondary antibodies for 1h at RT. Finally, membranes were washed with TBS-T and incubated with an ECL substrate (Thermo Fisher Scientific). The proteins were visualized using the MF-ChemiBIS 3.2 bioimaging system (Biostep, Germany). All unprocessed Western blot images are shown in Suppl. Fig. 10 and 11.

Subcellular protein fractionation

For separation of cytoplasmic, membrane and nuclear protein extracts of osteoblasts, primary murine osteoblasts were differentiated from the bone marrow of three WT mice. At day 7, cells were harvested and the subcellular protein fractions were isolated using the subcellular protein fractionation kit (Thermo Fisher Scientific) according to manufacturer`s recommendation.

Immunofluorescence staining

For immunofluorescence staining, cells were grown on glass slides. At the desired time point, cells were fixed with 100% methanol for 15 min, permeabilized with 0.5% Triton X-100 for 10 min and after washing for three times, blocked with 1% BSA in PBS for 30 min. Afterwards, cells were incubated with an anti-mouse Tfr2 antibody (H-140, Santa

Cruz) over night at 4 °C. After washing, cells were stained with an anti-mouse osterix antibody (sc-393325, Santa Cruz) or phalloidin at RT for 1 h. Subsequently, cells were washed and incubated for 1 h with an Alexa Fluor 488 or Alexa Fluor 594-labelled secondary antibody (Life Technologies), washed, and stained with DAPI for 5 min. After washing again, glass slides were embedded in a small droplet of mounting medium (Dako). Slides were examined using a Zeiss LSM 510 confocal microscope (Zeiss EC Plan-Neofluar 40x/1.3 Oil), and photographs were taken and processed with the Zen 2009 software.

Co-immunoprecipitation

Human hepatoma cells (HuH7) were transfected with 7.5 μg of pCMV-3XFLAG-BMPR-IA and 7.5 μg pcDNA3-TFR2-HA or pcDNA3-LDLR-HA using TransIT®-LT1 Transfection Reagent (Mirus Bio LLC) following the manufacture's protocol. Forty-eight hours after transfection cells were treated with 50 ng/ml of BMP-2 (Peprotech) for 1.5 h, where indicated. Cell lysates were incubated with pre-equilibrated anti-FLAG M2 affinity gel (Sigma Aldrich) at 4°C for 2 h. Samples were then eluted with 50 μl of lysis buffer containing 300 μg/ml 3X FLAG Peptide (Sigma Aldrich). 10% of the total lysate was used as input (In). Immunorecognition was visualized using αFLAG and αHA antibodies (1:1,000, Sigma Aldrich).

Next generation sequencing and data analysis

Total RNA was isolated from day 7 differentiated cells of *Tfr2*$^{-/-}$ and WT mice using Trifast. RNA quality was assessed using the Agilent Bioanalyzer and total RNA with an integrity number of ≥ 9 was used. mRNA was isolated from 1 μg total RNA using the NEBNext Poly(A) mRNA Magnetic Isolation Module according to the manufacturer's instructions. After chemical fragmentation, samples were subjected to strand-specific RNA-Seq library preparation (Ultra Directional RNA Library Prep, NEB). After ligation of adaptors (Oligo1 5'-ACA CTC TTT CCC TAC ACG ACG CTC TTC CGA TCT-3', Oligo2: 5'-P-GAT CGG AAG AGC ACA CGT CTG AAC TCC AGT CAC-3') residual oligos were depleted by bead purification (XP, Beckman Coulter). During subsequent PCR enrichment (15 cycles) libraries were indexed (Primer1: Oligo_Seq AAT GAT ACG GCG ACC ACC GAG ATC TAC ACT CTT TCC CTA CAC GAC GCT CTT CCG ATC T, primer2: GTG ACT GGA GTT CAG ACG TGT GCT CTT CCG ATC T, primer3: CAA GCA GAA GAC GGC ATA CGA GAT NNNNNN GTG ACT GGA GTT. After final purification (XP beads) libraries were quantified (Qubit dsDNA HS Assay Kit, Invitrogen), equimolarly pooled and distributed on multiple lanes for 75bp single read sequencing on a Illumina HiSeq 2500 and a Illumina NextSeq 500.

After sequencing, FastQC (http://www.bioinformatics.babraham.ac.uk/) was used for a basic quality control. Reads were then mapped onto the mouse genome (mm10) using GSNAP (version 2014-12-17) together with known splice sites (Ensembl v75) as support. Library diversity was assessed by investigating the redundancy in the mapped reads. A table with counts per gene was obtained by running featureCounts (v1.4.6) on the uniquely mapped reads using Ensembl v75 gene annotations. Normalization of the raw read counts based on the library size and testing for differential expression between the KO and WT was

performed with the R package DESeq2 (v1.6.3). Genes with an adjusted (Benjamini-Hochberg) p-value of less than 0.05 were considered as differentially expressed.

Gene ontology analyses were performed with Cytoscape 3.2.1 and the ClueGO plugin. Only significantly ($p<0.05$) up- or down-regulated genes were fed into the analyses. Gene Set Enrichment Analysis (GSEA) was carried out using the Broad Institute GSEA software "GseaPreRanked" tool (nperm=1000, set_min=5, set_max=500, scoring_scheme=weighted) to analyze a list of 18,106 non-redundant gene symbols ranked by their log2 fold-change of expression between *Tfr2*$^{-/-}$ and WT conditions. In total 58 gene sets were used for the analysis including 50 Hallmark gene sets, three osteoblast specific gene sets from Park et al. and Zaidi et al., and five other gene sets from Sanjuan-Pla et al.[70–72].

Expression of the Tfr2 extracellular domain

The coding sequence of the full-length extracellular domain (ECD, aa 103-798) of murine Tfr2 was synthesized by Genscript (Germany). Recombinant His-MBP-c3-Tfr2-ECD was expressed in Sf9 insect cells using the baculovirus expression system (pOCC211-Tfr2-ECD). Culture supernatant (5 liters) was harvested, filtered, and loaded on a HisTrap column, after extensive wash with PBS, the Tfr2-ECD protein was eluted using PBS with 250 mM imidazole. The yield in the first protein production was 40 mg and in the second 46 mg Tfr2-ECD. Presence of Tfr2 was analyzed using Coomassie staining of a SDS-PAGE with reducing conditions and Western blot.

Experiments were repeated with a commercially produced Tfr2-ECD from Cusabio. This fragment also contained the entire ECD (aa 103-798) and was dissolved in PBS only.

Surface plasmon resonance binding and kinetic analysis

Interactions of the Tfr2-ECD and holo-Tf, BMP ligands (BMP-2, -4, -6, -7, R&D Systems) and BMP receptors (BMPR-IA, BMPR-II, R&D Systems) were analyzed using a Biacore T100 instrument (GE Healthcare). Tfr2-ECD, BMP-2 and BMP-4 were immobilized onto Series S Sensor Chips C1 (GE Healthcare) via its amine groups at 25 °C. The carboxyl groups on the chip surface were activated for 7 min with a mixture containing 196 mM 1-ethyl-3-(3-dimethylaminopropyl) carbodiimide hydrochloride and 50 mM *N*-hydroxysuccinimide at a flow rate of 10 µl/min. Next 5 µg/ml of Tfr2-ECD diluted in sodium acetate buffer (pH 4.5) or 2 µg/ml BMP-2 or BMP-4 were injected at 5 µl/min flow rate until an immobilization levels of approx. 200 RU in case of Tfr2-ECD or 100 RU in case of BMP-2 and BMP-4 were achieved. Unreacted groups were deactivated via injection of 1 M ethanolamine-HCl, pH 8.5 (7 min, 10 µL/min). A reference surface was created according to the same protocol but omitting the Tfr2 injection.

The binding analysis was performed at 37 °C at a flow rate of 30 µl/min. Each analyte was diluted in running buffer (HBS-P (pH 7.4), 150 mM NaCl, supplemented with 50 nM $FeCl_3$). In some experiments, 500 mM NaCl were used to reduce potential non-specific binding. BMP ligands were used at the indicated concentrations (0-50 nM); BMP receptors at a concentration of 2-200 nM, holo-Tf at 2.5-100 µM and Tfr2-ECD at 10-5,000 nM. In some experiments, BMP-2/BMPR-IA and BMP-2/holo-Tf were injected at the same time.

Concentration-dependent binding of holo-Tf was performed without intermediate regeneration.

For binding analysis, an injection of analyte for 240 s or 300 s over a Tfr2-ECD surface was followed by 1000 s dissociation. The values of the binding levels were recorded from referenced signals 10 s before the end of injection relative to baseline response. They were then emended for the respective molecular weight. After dissociation for 1000 s, the chip surface was regenerated for 60 s with 5 M NaCl, 50 mM NaOH in HBS-P, followed by a 1000 s stabilization time.

Single cycle kinetics with five sequential analyte injections were carried out with a sensitivity enhanced Biacore T200 (GE Healthcare) to determine the Kd value range of Holo-Tf/Tfr2 and the dissociation rates k_{off} (complex stabilities) for Tfr2 binding to BMP-2 and BMP-4 surfaces. The kinetic fitting was performed by global fitting using the 1:1 Langmuir binding model (A + B = AB). Steady state analyses were conducted to determine the affinities (Kd). Therefore, a 1:1 interaction of Tfr2 with BMP-2 or BMP-4 was assumed by fitting the measured binding responses at equilibrium against the concentration. To achieve a robust fit and the typical curvature of the plot, a wide range of Tfr2 concentrations was analyzed (10-5000 nM). Binding and kinetic parameters were evaluated with Biacore™ T200 evaluation software 3.1.

BMP-2 competitive ELISA

The Duo Set BMP-2 ELISA kit from R&D Systems was used. After coating the plate with the BMP-2 capture antibody overnight, 1.5 ng/ml BMP-2 was added together with increasing concentrations of the Tfr2-ECD or the BMPR-IA (positive control, R&D Systems). After 1 h incubation at RT and extensive washing, the detection antibody was added according to the manufacturer´s protocol and the amount of BMP-2 was quantified. This experiment was performed at least three independent times.

Statistical analysis

Data are presented as mean ± standard deviation (SD). Graphs and statistics were prepared using the Graphpad Prism 6.0 software. Normality of data was determined using the Kolmogorov-Smirnov test. In case data were normally distributed, statistical evaluations of two group comparisons were performed using a two-sided Student’s t-test. One-way analysis of variance (ANOVA) was used for experiments with more than two groups. Two-way ANOVA with Bonferroni post-hoc tests was used for analyzing genotype and treatment effects. If data were not normally distributed, the Mann-Whitney test and the Wilcoxon signed rank test were used to analyze data. Frequency distributions of micromineralization densities from qBSE-SEM gray scale images were compared using the Kolmogorov-Smirnov test67.

Supplementary Material

Refer to Web version on PubMed Central for supplementary material.

Acknowledgements

We would like to thank our technicians for their excellent work. We thank the Core Facility Cellular Imaging of the TU Dresden for their support with the confocal microscope and the acquisition of immunofluorescence images and Dr. Anja Drescher and Dr. Joachim Nickel for critical suggestions regarding SPR analyses.

This work was supported by the German Research Foundation (DFG-SFB655 to LCH and UP; TRR-67 to VH and LCH; µBONE to MR and LCH; RA1923/12-1 to MR) and MedDrive start-up grants from the Medical Faculty of the Technische Universität Dresden (MR and UB). MR was supported by the Support-the-Best Initiative of the TUD funded through the Excellence initiative of the German Federal and State Governments. JHDB and GRW received a Wellcome Trust Joint Investigator Award (110141/Z/15/Z and 110140/Z/15/Z).

References

1. Muckenthaler MU, Rivella S, Hentze MW, Galy B. A Red Carpet for Iron Metabolism. Cell. 2017; 168:344–361. DOI: 10.1016/j.cell.2016.12.034 [PubMed: 28129536]
2. Imel EA, et al. Serum fibroblast growth factor 23, serum iron and bone mineral density in premenopausal women. Bone. 2016; 86:98–105. DOI: 10.1016/j.bone.2016.03.005 [PubMed: 26965530]
3. Guggenbuhl P, et al. Bone mineral density in men with genetic hemochromatosis and HFE gene mutation. Osteoporosis international : a journal established as result of cooperation between the European Foundation for Osteoporosis and the National Osteoporosis Foundation of the USA. 2005; 16:1809–1814. DOI: 10.1007/s00198-005-1934-0
4. Nemeth E, et al. Hepcidin regulates cellular iron efflux by binding to ferroportin and inducing its internalization. Science. 2004; 306:2090–2093. DOI: 10.1126/science.1104742 [PubMed: 15514116]
5. Powell LW, Seckington RC, Deugnier Y. Haemochromatosis. Lancet. 2016; 388:706–716. DOI: 10.1016/S0140-6736(15)01315-X [PubMed: 26975792]
6. Camaschella C, et al. The gene TFR2 is mutated in a new type of haemochromatosis mapping to 7q22. Nature genetics. 2000; 25:14–15. DOI: 10.1038/75534 [PubMed: 10802645]
7. Fleming RE, et al. Targeted mutagenesis of the murine transferrin receptor-2 gene produces hemochromatosis. Proceedings of the National Academy of Sciences of the United States of America. 2002; 99:10653–10658. DOI: 10.1073/pnas.162360699 [PubMed: 12134060]
8. Forejtnikova H, et al. Transferrin receptor 2 is a component of the erythropoietin receptor complex and is required for efficient erythropoiesis. Blood. 2010; 116:5357–5367. DOI: 10.1182/blood-2010-04-281360 [PubMed: 20826723]
9. Wallace DF, Summerville L, Lusby PE, Subramaniam VN. First phenotypic description of transferrin receptor 2 knockout mouse, and the role of hepcidin. Gut. 2005; 54:980–986. DOI: 10.1136/gut.2004.062018 [PubMed: 15951546]
10. Johnson MB, Enns CA. Diferric transferrin regulates transferrin receptor 2 protein stability. Blood. 2004; 104:4287–4293. DOI: 10.1182/blood-2004-06-2477 [PubMed: 15319290]
11. Poli M, et al. Transferrin receptor 2 and HFE regulate furin expression via mitogen-activated protein kinase/extracellular signal-regulated kinase (MAPK/Erk) signaling. Implications for transferrin-dependent hepcidin regulation. Haematologica. 2010; 95:1832–1840. DOI: 10.3324/haematol.2010.027003 [PubMed: 20634490]
12. D'Alessio F, Hentze MW, Muckenthaler MU. The hemochromatosis proteins HFE, TfR2, and HJV form a membrane-associated protein complex for hepcidin regulation. Journal of hepatology. 2012; 57:1052–1060. DOI: 10.1016/j.jhep.2012.06.015 [PubMed: 22728873]
13. Wallace DF, et al. Combined deletion of Hfe and transferrin receptor 2 in mice leads to marked dysregulation of hepcidin and iron overload. Hepatology. 2009; 50:1992–2000. DOI: 10.1002/hep.23198 [PubMed: 19824072]
14. Hogan BL. Bone morphogenetic proteins: multifunctional regulators of vertebrate development. Genes & development. 1996; 10:1580–1594. [PubMed: 8682290]
15. Andriopoulos B Jr, et al. BMP6 is a key endogenous regulator of hepcidin expression and iron metabolism. Nature genetics. 2009; 41:482–487. DOI: 10.1038/ng.335 [PubMed: 19252486]

16. Babitt JL, et al. Bone morphogenetic protein signaling by hemojuvelin regulates hepcidin expression. Nature genetics. 2006; 38:531–539. DOI: 10.1038/ng1777 [PubMed: 16604073]

17. Mayeur C, Leyton PA, Kolodziej SA, Yu B, Bloch KD. BMP type II receptors have redundant roles in the regulation of hepatic hepcidin gene expression and iron metabolism. Blood. 2014; 124:2116–2123. DOI: 10.1182/blood-2014-04-572644 [PubMed: 25075125]

18. Steinbicker AU, et al. Perturbation of hepcidin expression by BMP type I receptor deletion induces iron overload in mice. Blood. 2011; 118:4224–4230. DOI: 10.1182/blood-2011-03-339952 [PubMed: 21841161]

19. Wang RH, et al. A role of SMAD4 in iron metabolism through the positive regulation of hepcidin expression. Cell metabolism. 2005; 2:399–409. DOI: 10.1016/j.cmet.2005.10.010 [PubMed: 16330325]

20. Yu PB, et al. Dorsomorphin inhibits BMP signals required for embryogenesis and iron metabolism. Nature chemical biology. 2008; 4:33–41. DOI: 10.1038/nchembio.2007.54 [PubMed: 18026094]

21. Shore EM, et al. A recurrent mutation in the BMP type I receptor ACVR1 causes inherited and sporadic fibrodysplasia ossificans progressiva. Nature genetics. 2006; 38:525–527. DOI: 10.1038/ng1783 [PubMed: 16642017]

22. Wallace DF, et al. A critical role for murine transferrin receptor 2 in erythropoiesis during iron restriction. British journal of haematology. 2015; 168:891–901. DOI: 10.1111/bjh.13225 [PubMed: 25403101]

23. Nai A, et al. The erythroid function of transferrin receptor 2 revealed by Tmprss6 inactivation in different models of transferrin receptor 2 knockout mice. Haematologica. 2014; 99:1016–1021. DOI: 10.3324/haematol.2013.103143 [PubMed: 24658816]

24. Urist MR. Bone: formation by autoinduction. Science. 1965; 150:893–899. [PubMed: 5319761]

25. Roetto A, et al. Comparison of 3 Tfr2-deficient murine models suggests distinct functions for Tfr2-alpha and Tfr2-beta isoforms in different tissues. Blood. 2010; 115:3382–3389. DOI: 10.1182/blood-2009-09-240960 [PubMed: 20179178]

26. Herrmann T, et al. Iron overload in adult Hfe-deficient mice independent of changes in the steady-state expression of the duodenal iron transporters DMT1 and Ireg1/ferroportin. Journal of molecular medicine. 2004; 82:39–48. DOI: 10.1007/s00109-003-0508-x [PubMed: 14618243]

27. Altamura S, et al. Resistance of ferroportin to hepcidin binding causes exocrine pancreatic failure and fatal iron overload. Cell metabolism. 2014; 20:359–367. DOI: 10.1016/j.cmet.2014.07.007 [PubMed: 25100063]

28. Tsay J, et al. Bone loss caused by iron overload in a murine model: importance of oxidative stress. Blood. 2010; 116:2582–2589. DOI: 10.1182/blood-2009-12-260083 [PubMed: 20554970]

29. Rishi G, Secondes ES, Wallace DF, Subramaniam VN. Normal systemic iron homeostasis in mice with macrophage-specific deletion of transferrin receptor 2. American journal of physiology. Gastrointestinal and liver physiology. 2016; 310:G171–180. DOI: 10.1152/ajpgi.00291.2015 [PubMed: 26608187]

30. Kamiya N, et al. Wnt inhibitors Dkk1 and Sost are downstream targets of BMP signaling through the type IA receptor (BMPRIA) in osteoblasts. Journal of bone and mineral research : the official journal of the American Society for Bone and Mineral Research. 2010; 25:200–210. DOI: 10.1359/jbmr.090806

31. Simsek Kiper PO, et al. Cortical-Bone Fragility--Insights from sFRP4 Deficiency in Pyle's Disease. The New England journal of medicine. 2016; 374:2553–2562. DOI: 10.1056/NEJMoa1509342 [PubMed: 27355534]

32. Wosczyna MN, Biswas AA, Cogswell CA, Goldhamer DJ. Multipotent progenitors resident in the skeletal muscle interstitium exhibit robust BMP-dependent osteogenic activity and mediate heterotopic ossification. Journal of bone and mineral research : the official journal of the American Society for Bone and Mineral Research. 2012; 27:1004–1017. DOI: 10.1002/jbmr.1562

33. Shimono K, et al. Potent inhibition of heterotopic ossification by nuclear retinoic acid receptor-gamma agonists. Nature medicine. 2011; 17:454–460. DOI: 10.1038/nm.2334

34. Fransen M, et al. Safety and efficacy of routine postoperative ibuprofen for pain and disability related to ectopic bone formation after hip replacement surgery (HIPAID): randomised controlled trial. Bmj. 2006; 333:519.doi: 10.1136/bmj.38925.471146.4F [PubMed: 16885182]

35. Shen GS, et al. Hepcidin1 knockout mice display defects in bone microarchitecture and changes of bone formation markers. Calcified tissue international. 2014; 94:632–639. DOI: 10.1007/s00223-014-9845-8 [PubMed: 24652331]
36. Guggenbuhl P, et al. Bone status in a mouse model of genetic hemochromatosis. Osteoporosis international : a journal established as result of cooperation between the European Foundation for Osteoporosis and the National Osteoporosis Foundation of the USA. 2011; 22:2313–2319. DOI: 10.1007/s00198-010-1456-2
37. Doyard M, et al. Decreased Bone Formation Explains Osteoporosis in a Genetic Mouse Model of Hemochromatosiss. PloS one. 2016; 11:e0148292.doi: 10.1371/journal.pone.0148292 [PubMed: 26829642]
38. Calzolari A, et al. TfR2 localizes in lipid raft domains and is released in exosomes to activate signal transduction along the MAPK pathway. Journal of cell science. 2006; 119:4486–4498. DOI: 10.1242/jcs.03228 [PubMed: 17046995]
39. Keller S, Nickel J, Zhang JL, Sebald W, Mueller TD. Molecular recognition of BMP-2 and BMP receptor IA. Nature structural & molecular biology. 2004; 11:481–488. DOI: 10.1038/nsmb756
40. Yin H, Yeh LC, Hinck AP, Lee JC. Characterization of ligand-binding properties of the human BMP type II receptor extracellular domain. Journal of molecular biology. 2008; 378:191–203. DOI: 10.1016/j.jmb.2008.02.031 [PubMed: 18342887]
41. Canali S, Wang CY, Zumbrennen-Bullough KB, Bayer A, Babitt JL. Bone morphogenetic protein 2 controls iron homeostasis in mice independent of Bmp6. American journal of hematology. 2017; doi: 10.1002/ajh.24888
42. Koch PS, et al. Angiocrine Bmp2 signaling in murine liver controls normal iron homeostasis. Blood. 2017; 129:415–419. DOI: 10.1182/blood-2016-07-729822 [PubMed: 27903529]
43. Ramos E, et al. Evidence for distinct pathways of hepcidin regulation by acute and chronic iron loading in mice. Hepatology. 2011; 53:1333–1341. DOI: 10.1002/hep.24178 [PubMed: 21480335]
44. Li X, et al. Targeted deletion of the sclerostin gene in mice results in increased bone formation and bone strength. Journal of bone and mineral research : the official journal of the American Society for Bone and Mineral Research. 2008; 23:860–869. DOI: 10.1359/jbmr.080216
45. MacDonald BT, et al. Bone mass is inversely proportional to Dkk1 levels in mice. Bone. 2007; 41:331–339. DOI: 10.1016/j.bone.2007.05.009 [PubMed: 17613296]
46. van Bezooijen RL, et al. Sclerostin is an osteocyte-expressed negative regulator of bone formation, but not a classical BMP antagonist. The Journal of experimental medicine. 2004; 199:805–814. DOI: 10.1084/jem.20031454 [PubMed: 15024046]
47. Kamiya N, et al. BMP signaling negatively regulates bone mass through sclerostin by inhibiting the canonical Wnt pathway. Development. 2008; 135:3801–3811. DOI: 10.1242/dev.025825 [PubMed: 18927151]
48. Yu C, et al. Advanced oxidation protein products induce apoptosis, and upregulate sclerostin and RANKL expression, in osteocytic MLO-Y4 cells via JNK/p38 MAPK activation. Molecular medicine reports. 2017; 15:543–550. DOI: 10.3892/mmr.2016.6047 [PubMed: 28000869]
49. Croons V, Martinet W, Herman AG, Timmermans JP, De Meyer GR. The protein synthesis inhibitor anisomycin induces macrophage apoptosis in rabbit atherosclerotic plaques through p38 mitogen-activated protein kinase. The Journal of pharmacology and experimental therapeutics. 2009; 329:856–864. DOI: 10.1124/jpet.108.149948 [PubMed: 19286921]
50. Kamiya N, Kaartinen VM, Mishina Y. Loss-of-function of ACVR1 in osteoblasts increases bone mass and activates canonical Wnt signaling through suppression of Wnt inhibitors SOST and DKK1. Biochemical and biophysical research communications. 2011; 414:326–330. DOI: 10.1016/j.bbrc.2011.09.060 [PubMed: 21945937]
51. Biswas S, et al. BMPRIA is required for osteogenic differentiation and RANKL expression in adult bone marrow mesenchymal stromal cells. Scientific reports. 2018; 8:8475.doi: 10.1038/s41598-018-26820-8 [PubMed: 29855498]
52. Witcher PC, et al. Sclerostin neutralization unleashes the osteoanabolic effects of Dkk1 inhibition. JCI insight. 2018; 3doi: 10.1172/jci.insight.98673
53. Lowery JW, et al. Loss of BMPR2 leads to high bone mass due to increased osteoblast activity. Journal of cell science. 2015; 128:1308–1315. DOI: 10.1242/jcs.156737 [PubMed: 25663702]

54. Bao Q, et al. Disruption of bone morphogenetic protein type IA receptor in osteoblasts impairs bone quality and bone strength in mice. Cell and tissue research. 2018; doi: 10.1007/s00441-018-2873-3
55. Zhang Y, et al. Loss of BMP signaling through BMPR1A in osteoblasts leads to greater collagen cross-link maturation and material-level mechanical properties in mouse femoral trabecular compartments. Bone. 2016; 88:74–84. DOI: 10.1016/j.bone.2016.04.022 [PubMed: 27113526]
56. Forsberg JA, et al. Heterotopic ossification in high-energy wartime extremity injuries: prevalence and risk factors. The Journal of bone and joint surgery. American volume. 2009; 91:1084–1091. DOI: 10.2106/JBJS.H.00792 [PubMed: 19411456]
57. Regis D, Sandri A, Sambugaro E. Incidence of heterotopic ossification after surface and conventional total hip arthroplasty: a comparative study using anterolateral approach and indomethacin prophylaxis. BioMed research international. 2013; 2013doi: 10.1155/2013/293528
58. Chakkalakal SA, et al. Palovarotene Inhibits Heterotopic Ossification and Maintains Limb Mobility and Growth in Mice With the Human ACVR1(R206H) Fibrodysplasia Ossificans Progressiva (FOP) Mutation. Journal of bone and mineral research : the official journal of the American Society for Bone and Mineral Research. 2016; 31:1666–1675. DOI: 10.1002/jbmr.2820
59. Agarwal S, et al. mTOR inhibition and BMP signaling act synergistically to reduce muscle fibrosis and improve myofiber regeneration. JCI insight. 2016; 1:e89805.doi: 10.1172/jci.insight.89805 [PubMed: 27942591]
60. Hino K, et al. Activin-A enhances mTOR signaling to promote aberrant chondrogenesis in fibrodysplasia ossificans progressiva. The Journal of clinical investigation. 2017; 127:3339–3352. DOI: 10.1172/JCI93521 [PubMed: 28758906]
61. Rodda SJ, McMahon AP. Distinct roles for Hedgehog and canonical Wnt signaling in specification, differentiation and maintenance of osteoblast progenitors. Development. 2006; 133:3231–3244. DOI: 10.1242/dev.02480 [PubMed: 16854976]
62. Nakamura T, et al. Estrogen prevents bone loss via estrogen receptor alpha and induction of Fas ligand in osteoclasts. Cell. 2007; 130:811–823. DOI: 10.1016/j.cell.2007.07.025 [PubMed: 17803905]
63. Clausen BE, Burkhardt C, Reith W, Renkawitz R, Forster I. Conditional gene targeting in macrophages and granulocytes using LysMcre mice. Transgenic research. 1999; 8:265–277. [PubMed: 10621974]
64. Rhee Y, et al. PTH receptor signaling in osteocytes governs periosteal bone formation and intracortical remodeling. Journal of bone and mineral research : the official journal of the American Society for Bone and Mineral Research. 2011; 26:1035–1046. DOI: 10.1002/jbmr.304
65. Liu X, et al. A novel mouse model of trauma induced heterotopic ossification. Journal of orthopaedic research : official publication of the Orthopaedic Research Society. 2014; 32:183–188. DOI: 10.1002/jor.22500 [PubMed: 24136593]
66. Norden DM, et al. Ibuprofen ameliorates fatigue- and depressive-like behavior in tumor-bearing mice. Life sciences. 2015; 143:65–70. DOI: 10.1016/j.lfs.2015.10.020 [PubMed: 26498217]
67. Bassett JH, et al. Optimal bone strength and mineralization requires the type 2 iodothyronine deiodinase in osteoblasts. Proceedings of the National Academy of Sciences of the United States of America. 2010; 107:7604–7609. DOI: 10.1073/pnas.0911346107 [PubMed: 20368437]
68. Rauner M, et al. Increased EPO Levels Are Associated With Bone Loss in Mice Lacking PHD2 in EPO-Producing Cells. Journal of bone and mineral research : the official journal of the American Society for Bone and Mineral Research. 2016; 31:1877–1887. DOI: 10.1002/jbmr.2857
69. Theurl I, et al. On-demand erythrocyte disposal and iron recycling requires transient macrophages in the liver. Nature medicine. 2016; 22:945–951. DOI: 10.1038/nm.4146
70. Sanjuan-Pla A, et al. Platelet-biased stem cells reside at the apex of the haematopoietic stem-cell hierarchy. Nature. 2013; 502:232–236. DOI: 10.1038/nature12495 [PubMed: 23934107]
71. Mootha VK, et al. PGC-1alpha-responsive genes involved in oxidative phosphorylation are coordinately downregulated in human diabetes. Nature genetics. 2003; 34:267–273. DOI: 10.1038/ng1180 [PubMed: 12808457]
72. Subramanian A, et al. Gene set enrichment analysis: a knowledge-based approach for interpreting genome-wide expression profiles. Proceedings of the National Academy of Sciences of the United

States of America. 2005; 102:15545–15550. DOI: 10.1073/pnas.0506580102 [PubMed: 16199517]

Europe PMC Funders Author Manuscripts

Europe PMC Funders Author Manuscripts

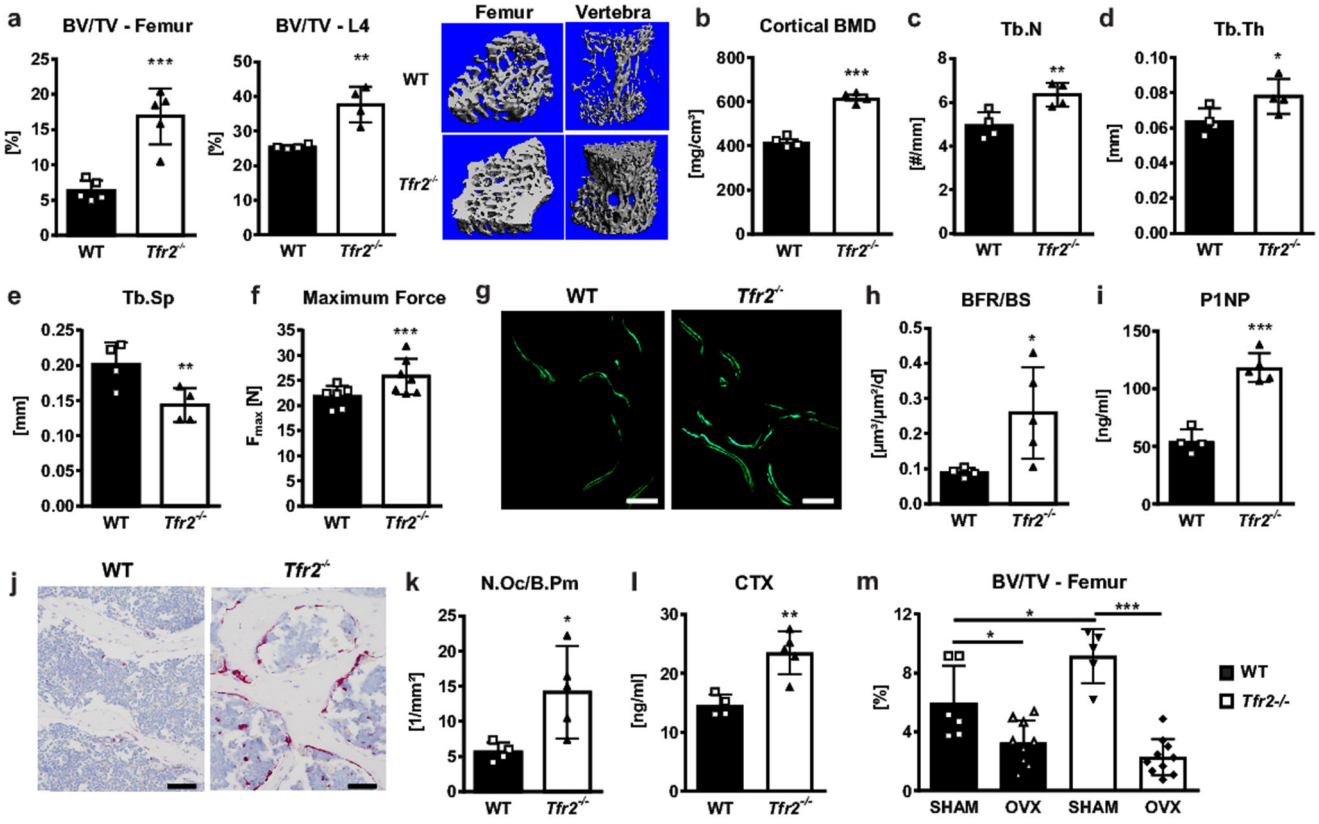

Figure 1. *Tfr2* deficiency results in high bone mass.

(a-l) The bones and serum bone turnover markers of ten-week-old male WT or *Tfr2*$^{-/-}$ mice were analyzed using µCT, histology, and ELISAs. (a) 3D reconstruction and quantitation of the bone volume/total volume (BV/TV) of the distal femur and the fourth vertebral body of WT and *Tfr2*$^{-/-}$ mice. Femur, n=5 per group; vertebral body, n=4 per group. (b) Cortical bone mineral density (BMD) at the femoral mid-shaft. n=4 per group. (c-e) Quantitation of vertebral trabecular number (Tb.N), trabecular thickness (Tb.Th), and trabecular separation (Tb.Sp). n=4 per group. (f) Maximum force at the femoral shaft assessed by 3-point-bending. (WT, n=6; Tfr2$^{-/-}$, n=7). (g) Representative histological sections from the third vertebral body of WT and *Tfr2*$^{-/-}$ mice showing calcein double staining. Bar indicates 100 µm. These experiments were repeated four times with similar results. (h) Quantification of the bone formation rate/bone surface (BFR/BS). (WT, n=4; Tfr2$^{-/-}$, n=5). (i) Quantification of serum P1NP as a marker of bone formation. (WT, n=4; Tfr2$^{-/-}$, n=5). (j) Representative histological tartrate-resistant acid phosphatase sections from the fourth vertebral body of WT and *Tfr2*$^{-/-}$ mice showing osteoclasts stained in pink. Bar indicates 100 µm. These examinations were performed four times with similar results. (k) Quantification of the number of osteoclasts/bone perimeter (N.Oc/B.Pm). (WT, n=4; Tfr2$^{-/-}$, n=5). (l) Quantification of serum CTX as a marker of bone resorption. (WT, n=4; Tfr2$^{-/-}$, n=5). (a-f, h-i, k-l) A two-tailed *t*-test was used for statistical analysis. (m) µCT analysis of femoral bone of 12-week-old sham-operated (SHAM) or ovariectomized (OVX) WT and *Tfr2*$^{-/-}$ mice. (WT Sham, n=6-10; WT OVX, n=9; Tfr2$^{-/-}$ Sham, n=5; Tfr2$^{-/-}$ OVX, n=10). Two-way

ANOVA with Bonferroni post-hoc test was used for statistical analysis. Data in all subpanels are presented as mean±SD with significances defined as *p<0.05, **p<0.01, ***p<0.001.

Europe PMC Funders Author Manuscripts

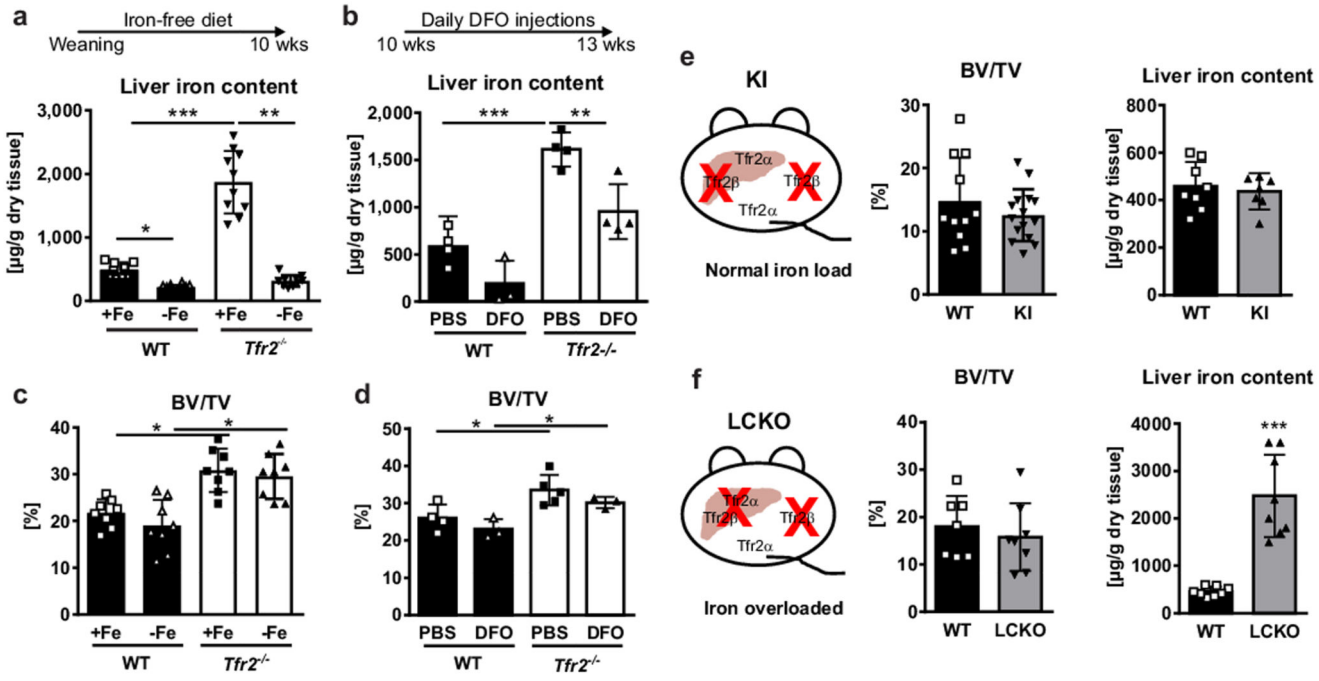

Figure 2. High bone mass in *Tfr2*$^{-/-}$ mice is independent of iron overload and the hepatic function of Tfr2.

(a, c) Male WT and *Tfr2*$^{-/-}$ mice received a purified diet without iron (-Fe) starting from weaning until the age of 10 weeks. Control mice received a standard diet with 0.2 g iron/kg food (+Fe). (a) Liver iron content was determined on dried tissue using photometry. (mean ±SD; n=10 per group). (c) Bone volume/total volume (BV/TV) was assessed using µCT. (mean±SD; WT +Fe n=9; WT –Fe, Tfr2$^{-/-}$ +Fe and Tfr2$^{-/-}$ -Fe, n=8 per group). (b, d) Ten-week-old female WT and *Tfr2*$^{-/-}$ mice received daily i.p injections of 250 mg/kg deferoxamine (DFO) or PBS for three weeks. At 13 weeks of age, mice were sacrificed to measure (b) iron liver content and (d) BV/TV. (n=3-5 per group). (a-d) Two-way ANOVA with Bonferroni post-hoc test was used for statistical analysis. (e) Schematic representation of *Tfr2* knock-in (KI) mice, which lack the *Tfr2β* isoform. BV/TV and iron liver content of 10-week-old male *Tfr2* KI mice and control mice. (BV/TV, WT n=11, KI n=15; Liver iron, WT n=8, KI n=7). (f) Schematic representation of the Tfr2 setup of liver-specific *Tfr2α* knock-out (LCKO) mice on a *Tfr2* KI background. BV/TV and liver iron content of 10-week-old male LCKO and WT mice. (n=8 per group). (e,f) A two-tailed *t*-test was used for statistical analysis. All data are presented as mean±SD. *p<0.05; **p<0.01; ***p<0.001.

Europe PMC Funders Author Manuscripts

Europe PMC Funders Author Manuscripts

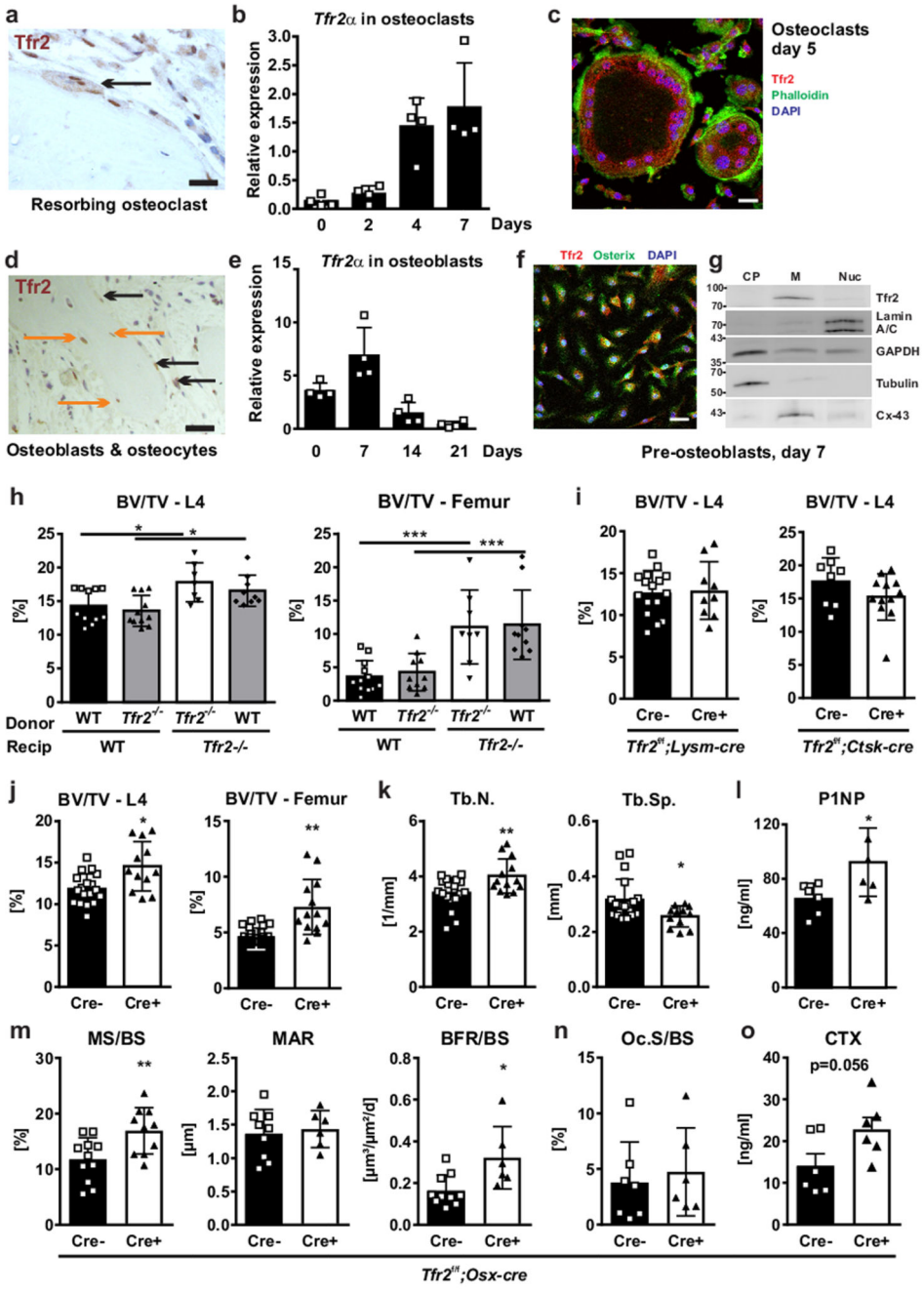

Figure 3. Deficiency of *Tfr2* in osteogenic cells increases bone mass.

(a, d) Immunohistochemical analysis of Tfr2 on vertebral bone of WT mice. One representative image is shown out of three. Arrows indicate Tfr2 expression in multinucleated osteoclasts and osteoblasts/osteocytes (osteoblasts: black arrows; osteocytes: orange arrows). Scale bar: 20 μm. (b, e) *Tfr2α* mRNA expression during osteoclast (b) and osteoblast (e) differentiation of WT cells (n=4). (c, f) Immunofluorescence staining for Tfr2 in mature osteoclasts (c) and immature osteoblasts (f). Scale bar: 20 μm. These staining were repeated twice with similar results. (g) Subcellular fractioning of day 7 osteoblast protein

lysates from WT mice. One representative blot is shown out of three. CP: cytoplasm; M: membrane; Nuc: nuclear fraction. Cx-43: connexin-43. (h) Bone marrow was transplanted from 12-week-old male WT or *Tfr2*$^{-/-}$ mice into lethally irradiated 9-week-old male WT and *Tfr2*$^{-/-}$ recipient (recip) mice. After 16 weeks, the bone volume/total volume (BV/TV) was measured using μCT. (L4, WT-WT n=11, Tfr2$^{-/-}$-WT n=11, Tfr2$^{-/-}$-Tfr2$^{-/-}$ n=7, WT-Tfr2$^{-/-}$ n=9; Femur, WT-WT n=12, Tfr2$^{-/-}$-WT n=10, Tfr2$^{-/-}$-Tfr2$^{-/-}$ n=8, WT-Tfr2$^{-/-}$ n=10). Two-way ANOVA with Bonferroni post-hoc test was used for statistical analysis. (i) BV/TV of the fourth lumbar vertebrae of 10-week-old male cre-positive and cre-negative *Tfr2*$^{f/f}$;*Lysm-Cre* and *Tfr2*$^{f/f}$;*Ctsk-Cre* mice. (Tfr2$^{f/f}$; Lysm-cre, Cre- n=16, Cre+ n= 9; Tfr2$^{f/f}$; CtskCre, Cre- n=8, Cre+ n=12). (j-o) Bone analysis of 10-week-old male cre-positive and cre-negative littermate control *Tfr2*$^{f/f}$;*Osx-Cre* mice. (j) BV/TV (L4, Cre- n=18, Cre+ n=12; Femur, Cre- n=18, Cre+ n=13). (k) Trabecular number (Tb.N) and trabecular separation (Tb.Sp) (Tb.N., Cre- n=18, Cre+ n=13; Tb.Sp., Cre- n=19, Cre+ n=12). (l) Serum levels of P1NP. (n=6 per group). (m) Mineralizing surface per bone surface (MS/BS), mineral apposition rate (MAR), and bone formation rate per bone surface (BFR/BS) determined at the lumbar spine. (MS/BS, Cre- n=11, Cre+ n=10; MAR, Cre- n=9, Cre+ n=6; BFR, Cre- n=10, Cre+ n=6). (n) Osteoclast surface per bone surface (Oc.S/BS) analyzed at the lumbar spine. (Cre- n=7, Cre+ n=6). (o) Serum CTX levels (n=6 per group). (i-o) A two-tailed *t*-test was used for statistical analysis. All data are presented as mean±SD. *p<0.05; **p<0.01; ***p<0.001.

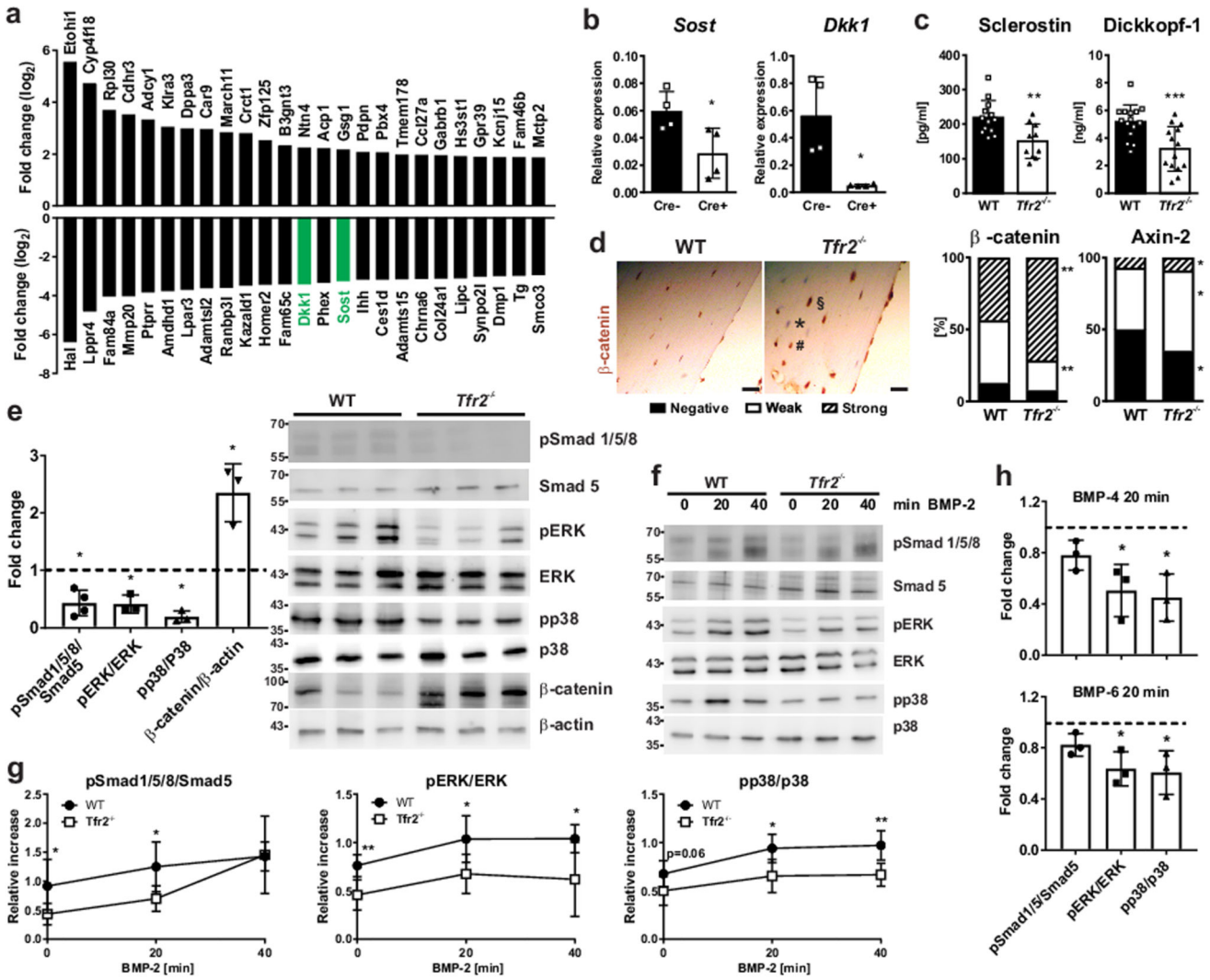

Figure 4. Down-regulation of BMP signaling and Wnt inhibitors in *Tfr2*-deficiency.

(a) Top 25 most increased and decreased genes as identified using next generation sequencing of day 7 osteoblasts from WT and *Tfr2*$^{-/-}$ mice (n=4 per genotype). (b) Gene expression of *Dkk1* and *Sost* in day 7 differentiated osteoblasts from *Tfr2*$^{f/f}$;*Osx-Cre* mice and littermate controls. Normalized to β-actin. (n=4 per group). (c) Serum concentrations of Dickkopf-1 and sclerostin in WT and *Tfr2*$^{-/-}$ mice. (sclerostin, WT n=13, Tfr2$^{-/-}$ n=10; Dickkopf, WT n=15, Tfr2$^{-/-}$ n=14). (d) Immunohistochemical analysis of β-catenin and axin-2 on femoral bone sections from WT and *Tfr2*$^{-/-}$ mice. Scale bar: 20 μm. Cells were quantified according to their staining intensity (negative (exemplified with an asterisk), weak (hash), strong (section mark)). (n=9 per group). (e) Analysis of the status of activated Smad and MAPK signaling in *ex vivo* differentiated osteoblasts (day 7) from *Tfr2*$^{-/-}$ mice normalized to WT osteoblasts. Phosphorylated proteins were normalized to their unphosphorylated counterparts. Expression of β-catenin was normalized to β-actin. Quantification is the result of densitometry of 5 independent Western blot experiments. Dotted line represents the WT level. (Smad1/5/8 n=4; pERK, pp38 and ß-catenin n=3). (f-g)

Ex vivo differentiated osteoblasts from WT and *Tfr2*$^{-/-}$ mice were treated with 50 ng/ml BMP-2 for 0-20-40 min. After protein extraction, phosphorylation of signaling proteins was analyzed using Western blot (f). (g) Graphs represent the quantification of 4 independent experiments. (n=4 per group). (h) Induction of Smad1/5, ERK, and p38 in WT and *Tfr2*$^{-/-}$ osteoblasts after 20 min of stimulation with 50 ng/ml BMP-4 or BMP-6. Dotted line represents the WT level. (n=3 per group). (b-e, g-h) A two-tailed *t*-test was used for statistical analysis. All data are presented as mean±SD (expect for (d), which shows percentages). *p<0.05; **p<0.01; ***p<0.001.

Europe PMC Funders Author Manuscripts

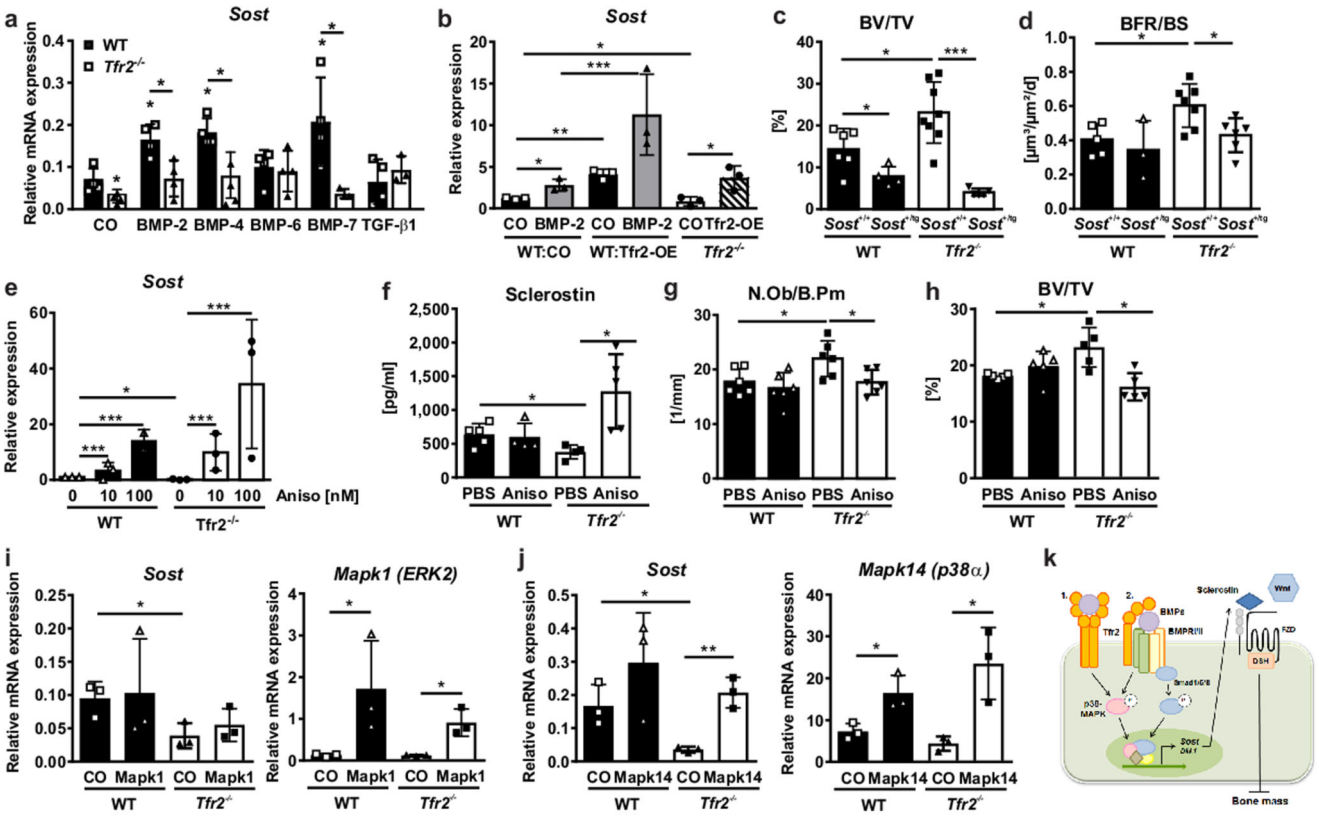

Figure 5. High bone mass in *Tfr2*-deficiency is rescued by overexpressing *SOST* or reactivating MAPK signaling.

(a) WT or *Tfr2*$^{-/-}$ osteoblasts were differentiated for 7 days and stimulated with 50 ng/ml BMPs or TGF-β1 for 48 h. *Sost* mRNA expression was determined using qPCR. (n=4). A two-tailed *t*-test was used for statistical analysis. (b) Day 7 WT or *Tfr2*$^{-/-}$ osteoblasts were transfected with an empty pcDNA3.1 vector (CO) or a pcDNA3.1 vector containing the Tfr2 gene (Tfr2-OE). Cells were either treated with 50 ng/ml BMP-2 or PBS. After 48 h, mRNA expression of *Sost* was determined using qPCR. (n=3). (c) Bone volume/total volume (BV/TV), WT/Sost$^{+/+}$ n=6, WT Sost$^{+/tg}$ n=4, Tfr2$^{-/-}$ Sost$^{+/+}$ n=8, Tfr2$^{-/-}$ Sost$^{+/tg}$ n=5 and (d) bone formation rate/bone surface (BFR/BS) of 10-week-old female *Tfr2*$^{-/-}$ or WT mice containing one (*SOST*$^{+/tg}$) or no allele (*SOST*$^{+/+}$) of the *SOST* transgene. (WT/Sost$^{+/+}$ n=5, WT/Sost$^{+/tg}$ n=3, Tfr2$^{-/-}$/Sost$^{+/+}$ n=7, Tfr2$^{-/-}$/Sost$^{+/tg}$ n=6). (b-d) Two-way ANOVA with Bonferroni post-hoc test was used for statistical analysis. (e) *Sost* mRNA expression in *ex vivo* differentiated osteoblasts from WT or *Tfr2*$^{-/-}$ mice after 24 h of anisomycin treatment (100 nM). (n=3 per group). One-way ANOVA with used for statistical analysis. (f-h) 10-week-old male WT and *Tfr2*$^{-/-}$ mice were treated with 5 mg/kg anisomycin for 3 weeks. Shown are the (f) serum levels of sclerostin (WT/PBS n=5, WT/Aniso n=4, Tfr2$^{-/-}$/PBS n=4, Tfr2$^{-/-}$/Aniso n=5). (g) Number of osteoblasts/bone perimeter (N.Ob/B.Pm) (n=6 per group), and (h) BV/TV of the fourth lumbar vertebrae. (n=5 per group). (i-j) Overexpression of ERK2 (pCMV6-Mapk1) and p38α (pCMV6-Mapk14) in day 7 WT and *Tfr2*$^{-/-}$ osteoblasts. *Sost* expression was analyzed after 48 h and normalized to β-actin. (n=3). (f-j) Two-way ANOVA with Bonferroni post-hoc test was used for statistical analysis. All data are presented as

Europe PMC Funders Author Manuscripts

mean±SD. *p<0.05; **p<0.01; ***p<0.001. (k) Scheme of Tfr2 actions in osteoblasts: Tfr2 binds BMPs and either directly activates BMP/MAPK signaling (1.) or activates them via binding to BMPR (2.) to induce the transcription of *Sost* and *Dkk1*. Secreted sclerostin acts as a Wnt antagonist and inhibits bone formation and decreases bone mass.

Europe PMC Funders Author Manuscripts

Europe PMC Funders Author Manuscripts

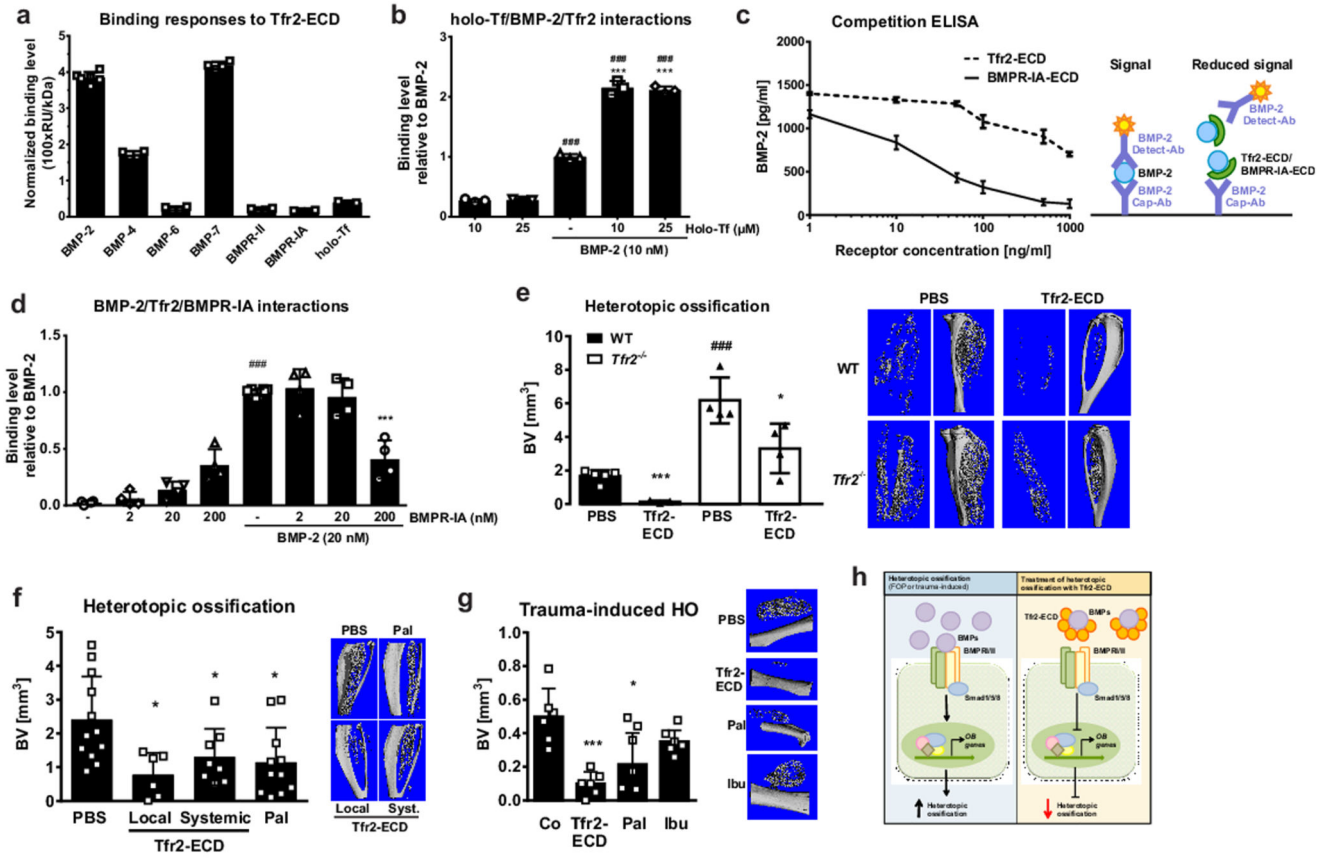

Figure 6. Tfr2 binds BMP ligands and blocks heterotopic ossification (HO).

(a-b) Surface plasmon resonance (SPR) experiments using Tfr2-ECD immobilized on the sensor chip and 1 mg/ml holo-transferrin (holo-Tf), different BMP ligands (50 nM), or 200 nM BMP receptors as analytes. All experiments were performed three independent times. (a) Quantification of the binding level normalized to the molecular weight. (BMP-2 n=6, BMP-4, 6, 7, BMPR-II and BMPR-IA n=4 per group, holo-Tf n=3). (b) Binding response of different concentrations of holo-Tf and/or BMP-2. (n=3; $^{###}$p<0.001 vs. holo-Tf alone; ***p<0.001 vs. BMP-2 alone). (c) Competitive BMP-2 sandwich ELISA was performed to test Tfr2-ECD (or BMPR-IA as a positive control) binding to BMP-2. A defined concentration of BMP-2 (1,500 pg/ml) was used with increasing concentrations of Tfr2-ECD and BMPR-IA. The principle of the assays is shown in the right schematic. (n=4). (d) SPR analyses. BMP-2 was injected either alone or with increasing concentrations of BMPR-IA. Binding response is relative to BMP-2 alone. (n=4; $^{###}$p<0.001 vs. BMPR-IA alone; ***p<0.001 vs. BMP-2 alone). (b, d) One-way ANOVA was used for statistical analysis. (e) HO in 12-week-old female WT and Tfr2$^{-/-}$ mice after two weeks quantified by µCT (without the bone volume of the tibia). Representative images are shown at the right. (WT PBS n=5, WT Tfr2-ECD n=3, Tfr2$^{-/-}$ PBS n=4, Tfr2$^{-/-}$ Tfr2-ECD n=4; *p<0.05; ***p<0.001 to respective PBS control; $^{###}$p<0.001 vs. WT). Two-way ANOVA with Bonferroni post-hoc test was used for statistical analysis. (f) HO in 12-week-old female WT mice after two weeks quantified by µCT (without the bone volume of the tibia). (PBS n=12, local Tfr2-ECD n=6, systemic Tfr2-ECD n=8, Pal n=11; *p<0.05 vs. PBS control). (g) Trauma-

induced HO model in 12-week-old female WT mice. HO after three weeks assessed using μCT. (n=6 per group; *p<0.05, ***p<0.001 vs. PBS control). (f, g) One-way ANOVA was used for statistical analysis. All data are presented as mean±SD. (h) Scheme of the mode of action of the Tfr2-ECD in the treatment of HO. Left: HO is induced by overactive BMP signaling, leading to the induction of osteoblastic genes and bone formation. Right: Tfr2-ECD neutralizes BMPs, preventing them from activating BMP signaling. Thus, osteoblastic bone formation is inhibited.

Europe PMC Funders Author Manuscripts